



## CloudRoots: Integration of advanced instrumental techniques and process modelling of sub-hourly and sub-kilometre land-atmosphere interactions

5 Jordi Vilà-Guerau de Arellano<sup>1</sup>, Patrizia Ney<sup>2</sup>, Oscar Hartogensis<sup>1</sup>, Hugo de Boer<sup>3</sup>, Kevin van Diepen<sup>1</sup>,  
Dzhaner Emin<sup>4</sup>, Geiske de Groot<sup>1</sup>, Anne Klosterhalfen<sup>5</sup>, Matthias Langensiepen<sup>6</sup>, Maria Matveeva<sup>4</sup>,  
Gabriela Miranda<sup>1</sup>, Arnold Moene<sup>1</sup>, Uwe Rascher<sup>4</sup>, Thomas Röckmann<sup>7</sup>, Getachew Adnew<sup>7</sup>, Alexander  
Graf<sup>2</sup>

<sup>1</sup>Meteorology and Air Quality Section, Wageningen University Research, 6708 PB Wageningen, the Netherlands

10 <sup>2</sup>Institute of Bio- and Geosciences, IBG-3: Agrosphere, Forschungszentrum Jülich GmbH, 52425 Jülich, Germany

<sup>3</sup>Department of Environmental Sciences, Faculty of Geosciences, Utrecht University, the Netherlands

<sup>4</sup>Institute of Bio- and Geosciences, IBG-2: Plant Sciences Forschungszentrum Jülich GmbH, 52425 Jülich, Germany

<sup>5</sup>Department of Forest Ecology & Management, Swedish University of Agricultural Sciences, 90183 Umeå, Sweden

<sup>6</sup>Faculty of Agriculture, University of Bonn, 53115 Bonn, Germany

15 <sup>7</sup>Institute of Marine and Atmospheric Research Utrecht University, 3584 CC Utrecht, The Netherlands

*Correspondence to:* Jordi Vilà-Guerau de Arellano (jordi.vila@wur.nl)

**Abstract.** The CloudRoots field experiment was designed to obtain a comprehensive observational data set that includes soil, plant and atmospheric variables to investigate the interaction between a heterogeneous land surface and its overlying  
20 atmospheric boundary layer at the sub-hourly and sub-kilometre scale. Our findings demonstrate the need to include measurements at leaf level in order to obtain accurate parameters for the mechanistic representation of photosynthesis and stomatal aperture. Once the new parameters are implemented, the mechanistic model reproduces satisfactorily the stomatal leaf conductance and the leaf-level photosynthesis. At the canopy scale, we find a consistent diurnal pattern on the contributions of plant transpiration and soil evaporation using different measurement techniques. From the high frequency  
25 and vertical resolution state variables and CO<sub>2</sub> measurements, we infer a profile of the plant assimilation that shows a strong non-linear behaviour. Observations taken by a laser scintillometer allow us to quantify the non-steadiness of the surface turbulent fluxes during the rapid changes driven by perturbation of the photosynthetically active radiation (PAR) by clouds, the so-called cloud flecks. More specifically, we find two-minute delays between the cloud radiation perturbation and ET. The impact of surface heterogeneity was further studied using ET estimates infer from the sun-induced fluorescence data and  
30 show small variation of ET in spite of the plant functional type differences. To study the relevance of advection and surface heterogeneity on the land-atmosphere interaction, we employ a coupled surface-atmospheric conceptual model that integrates the surface and upper-air observations taken at different scales: from the leaf-level to the landscape. At the landscape scale, we obtain the representative sensible heat flux that is consistent with the evolution of the boundary-layer depth evolution. Finally, throughout the entire growing season, the wide variations in stomatal opening and photosynthesis  
35 lead to large variations of plant transpiration at the leaf and canopy scales. The use of different instrumental techniques



enables us to compare the total ET at various growing stages, from booting to senescence. There is satisfactory agreement between evapotranspiration of total ET, but the values remain sensitive to the scale at which ET is measured or modelled.

## 1. Introduction

Evapotranspiration (ET), the net exchange of water vapour between the land and the atmosphere, remains an elusive process to be measured, quantified and represented in models (Katul, et al., 2012). ET is a key variable in the exchange of heat, moisture and carbon dioxide at the surface and it strongly depends on how radiation and energy are partitioned (Moene and Dam, 2014; Monson and Baldocchi, 2014). The amounts of direct and diffuse radiation reaching the leaves depend on the transfer of radiation that is strongly perturbed by clouds and aerosols, and on its subsequent penetration into the canopy. Triggered by these ambient light conditions, the stomatal responses and the surface and boundary-layer dynamics are the other two key drivers that regulate how the net available radiative energy is partitioned between the turbulent sensible and latent heat fluxes (van Heerwaarden and Teuling, 2014). However, due to the highly non-stationary nature of atmospheric radiation (van Kesteren, et al., 2013b) and turbulent nature of the meteorological fluctuations, we still lack fundamental understanding on the two-way feedback between stomatal control and cloud radiation perturbations across scales and land/atmosphere conditions (Katul, et al., 2012; Sikma, et al., 2018).

The bi-directional link between surface processes and boundary layer clouds as described above is what we refer to as the CloudRoots concept, where clouds are rooted in, or coupled to, the surface and vice-versa (Vilà-Guerau de Arellano et al, 2014). The degree of coupling depends on soil, plant, boundary-layer dynamics and weather conditions such as wind (Sikma et al., 2018). To fully comprehend this system requires inclusion of all necessary parameters at the required spatial scales, from the size of the stomata (10 - 100 $\mu$ m) to the depth of the boundary layer and cloud top (~3 km), temporal scales from seconds to daily and seasonal cycles and across disciplines bringing together experts from ecophysiology to turbulence. This can only be obtained by integrating experimental and modelling efforts. It is the main goal of this paper to describe and show first results of our first CloudRoots field experiment aimed at obtaining new understanding on the interaction between the soil, vegetation and the clear/cloudy boundary layers at these sub-hourly and sub-kilometre scales, *i.e.* on spatiotemporal scales smaller than the characteristic grid resolution scales of the weather and climate models.

Thanks to their high-quality routine measurement program (Franz, et al., 2018; Rebmann, et al., 2018), ICOS sites lend themselves as anchors for additional experiments. Here, we describe the CloudRoots campaign near the agricultural site Selhausen (ICOS site DE-RuS) and the Jülich Observatory for Cloud Evolution – Core Facility (JOYCE, <http://joyce.cloud>) in Germany during spring 2018 (Löhnert, et al., 2015). In order to quantify all the necessary scales of interest; leaf, canopy and landscape, we complemented the existing radiation, flux and soil measurements of the ICOS site by scintillometry, microlysimeters, sap-flow and leaf-level flux measurements, quasi-instantaneous vertical profiles and spectroscopic measurements of vegetation indices and sun-induced fluorescence (SIF). Scintillometers provided minute-scale turbulent fluxes enabling us to connect stomatal responses to the energy, moisture and CO<sub>2</sub> fluxes at this timescale. Microlysimeters,



soil flux chambers, sap-flow, leaf-level chambers and canopy-resolving profile all have the ability to distinguish vegetation from soil CO<sub>2</sub> and H<sub>2</sub>O fluxes in contrast to the eddy-covariance technique that provided net fluxes from the two sources combined. The remote sensing measurements of boundary-layer dynamic evolution and cloud properties made at JOYCE provided evidence on diurnal variations of the boundary-layer depth, the role of entrainment and cloud diurnal variability. A key aspect of the research strategy of CloudRoots is the integration of all these measurements in a land-atmosphere conceptual model CLASS (Vilà-Guerau de Arellano, et al., 2015). This model has been specially developed to support the interpretation of measurements at the sub-hourly scales (Vilà-Guerau de Arellano, et al., 2019).

To this end, we study the following five facets of the diurnal interactions between the land and the atmosphere: (i) observational validation at leaf level of the mechanistic model representation of the stomatal aperture and photosynthesis, (ii) the CO<sub>2</sub>-H<sub>2</sub>O flux partition diurnal variability due to the soil and plant contributions at the canopy level, (iii) the non-steadiness of these fluxes due to the influence of clouds, (iv) the spatial heterogeneity of ET inferred from the SIF measurements and (v) the integration of the observations in the conceptual model CLASS to quantify the influence of advection. We finally obtain a daily estimation of ET and discussed differences with respect to the observational or modelling techniques.

The paper is organized as follows. In Section 2 we give a detailed overview of the field-experiment with special emphasis on the instrumentation used that serve the overall goals of our CloudRoots concept. The results Section 3 is organized along the five topics outlined above. First, at leaf level, we first validate a photosynthesis-conductance mechanistic model that is commonly used in large-eddy simulations (Pedruzo-Bagazgoitia, et al., 2017; Sikma, et al., 2018) and the global numerical model prediction system IFS-ECMWF (Boussetta, et al., 2013). This allows us to assess the need to revisit currently used constants in the mechanistic model representing photosynthesis. This part is completed by comparing leaf transpiration rate with tiller-level measurements of sap flow evaporation at different stages of the growing season. Second, and in order to scale up to the canopy level, we analyse the soil and plant partitioning of the net evapotranspiration and net ecosystem exchange (NEE) based on the inversion of observed high-resolution vertical concentration profiles (Warland and Thurtell, 2000; Santos, et al., 2011). Third, in analysing the impact of clouds on evapotranspiration, we measure the potential effectiveness of diffuse radiation in enhancing ET (Kanniah, et al., 2012). Extending previous work by van Kesteren et al. (2013b), we quantify the time-lag between fluctuations in incoming shortwave radiation and ET in the field. These real-world measurements are an essential addition to time-lag of plant responses to radiation changes studied in laboratory experiments (Vico, et al., 2011). Fourth, we infer the spatial variability of ET around the CloudRoots site using SIF remote-sensing observations. Fifth, all these observations are then integrated in several numerical experiments made by CLASS with special emphasize on the treatment and role of how to include surface heterogeneity and heat/moisture advection to improve the interpretation of the observations. Finally, in the discussion Section 4 we bring together and discuss all CloudRoots methodologies by comparing their daily ET estimates. Conclusions are given in Section 5.



## 2. Description of the Cloud Roots field experiment and modelling effort

### 2.1 Site description

The CloudRoots field campaign was carried out at the Terrestrial Environmental Observatory (TERENO) Selhausen, which is located in the southern part of the Lower Rhine Embayment in Western Germany (50°52'09"N, 6°27'01"E, 104.5 m a. s. l.) in a region largely dominated by agriculture (Fig. 1). In 2011, the site was equipped with micrometeorological measurement devices for long-term monitoring of energy and carbon exchange. Since 2015, the station has been extended in accordance with ICOS standards for Level 1 sites (ICOS site code DE-RuS) (Ney, 2019). For this campaign, a further IRGASON eddy-covariance (EC) system with an open path gas analyser (see Sect. 3.4) was placed on the test field and used for additional flux measurements presented here.

The test field covers 9.8 ha and is surrounded by other croplands (Ney & Graf, 2018). As Fig. 1 shows, these cultivated areas comprise mainly winter wheat, winter barley, sugar beet, rapeseed, maize, potatoes and peas, whereby the various field sizes and locations of crops has led to small-scale heterogeneity in the vegetation cover. An agricultural road, mainly used by farm machinery, passes by the northern edge of the field. The next inhabited settlement is located 500 m to the west (Fig. 1). There are two lignite open-cast mines in the wider surrounding of the study site, located 6 km northeast (extension of 4400 ha with a maximum depth of 470 m b. g. l.) and 6 km west (extension of 1400 ha with a maximum depth of 200 m b. g. l.). In general, the land surface at the study site is flat and has a slope less than 4°. A loess layer with a thickness of about 1 m covers Quaternary sediments, which were mainly built-up from fluvial deposits of the Ruhr river system. The overlying soil is an Orthic Luvisol according to the USDA classification (IUSS Working Group WRB, 2006), whose texture is silt loam with a mixture of 14% clay, 73% silt and 13% sand (Schmidt, et al., 2012).

The local climate is classified as temperate maritime with an annual mean air temperature of 10.3°C and an annual mean precipitation of 718 mm (reference period 1981-2010, data taken from the DWD climate station of the Forschungszentrum Jülich 5.3 km distant from the test site). The observation period from beginning of May until end of June 2018 was characterized by a 2.9°C higher mean air temperature (17.5°C) and 46% less precipitation in comparison to the long-term average.

The field campaign covered the main growing phases (booting, heading and maturity stage) of winter wheat. During the observation period, we monitored three intensive observation periods (IOP), during which complementary measurements using microlysimeters, leaf-level measurements, SIF measurements on canopy and regional scale, as well as vertical profiles within and above the canopy were performed. Fig. 2 shows a timeline of the deployment of the campaign-specific measurement setup (see Sect. 3.4) that includes the IOPs on 7<sup>th</sup> May (IOP 1), 15<sup>th</sup> (IOP 2) and 28<sup>th</sup> June 2018 (IOP 3). The main meteorological and biometric conditions are summarized in Table 1. The test field was cultivated with a crop rotation cycle typical of the region (Ney, 2019). The rotation prior to the observation period was beet/potatoes/winter wheat (catch-crop) and sugar beet. Residues of the harvest of sugar beet were left on the site and ploughed in before the cultivation cycle started with the sowing of winter wheat (*Triticum aestivum* L.; variety Premio) in October 2017. The field was fertilized with



mineral nitrogen (N) once in March, April and May 2018 (81.6, 39.2 and 50 kg N ha<sup>-1</sup>). The wheat was harvested on 17 July 2018 with a yield of 92 dt ha<sup>-1</sup>. A detailed overview of the field management activities in place before, during and after the campaign is given in the Appendix (Table A1).

## 2.2 Weather and crop description during the IOPs

5 The weather situation during all three IOPs was mainly characterized by an anticyclonic pressure pattern over Central Europe (IOP 1 and IOP 2), extending up to Northern Europe during IOP 3, which lead to high 2 m-temperatures up to 24 to 26°C during IOP 1 and IOP 2, and 28°C during IOP 3, (Table 1). Cloudiness and temperature-inversion heights at the top of the atmospheric boundary layer were different. While weak subsidence motions during IOP 1 led to a slightly rising temperature-inversion layer between 1200 to 2000 m a. g. l. with clear conditions during the whole period (mean daytime global radiation  $S_{\downarrow}$  of 514 W m<sup>-2</sup>), a weak cold front passed the measuring site from the northwest in the early morning of IOP 2 (mean daytime  $S_{\downarrow}$  of 311 W m<sup>-2</sup>). Diurnal heating caused the replacement of a layer of stratocumulus at a height of 1800 m a. g. l., in the morning, followed by the appearance of scattered towering cumulus clouds. Light showers occurred only in the vicinity of the site. During IOP 3, a few shallow cumulus and cirrus clouds appeared, despite the existence of a small upper-air low which passed the area around the edge of a larger cut-off, although it was located above South-Eastern Europe. The mixed boundary layer was topped at a height of around 1700 m a. g. l.

The persistent high-pressure weather conditions resulted in a drought during the entire observation period. Ongoing dryness led to a reduction in the soil water content at 20 cm depth (Table 1) from 27 vol.% during IOP 1 to 15 vol.% at IOP 3. The development of the winter wheat was influenced by the current conditions to the extent that maturity occurred, more than 14 days earlier than in previous years. The leaf area index (LAI) ranged from 4.5 (green growing stage) m<sup>2</sup> m<sup>-2</sup> in IOP 1 to 5.5 m<sup>2</sup> m<sup>-2</sup> IOP 2 (green/yellow ripening stage). No changes in LAI were observed between IOP 2 and IOP 3 (yellow/senescence stage).

## 2.3 Instrument description

Table 2 summarizes all the variables measured and modelled during CloudRoots, together with specific nomenclature and information on units and scales.

### 2.3.1 Microlysimeters

For direct measurements of soil evaporation ( $E_{\text{lys}}$ ), four microlysimeters were installed at a number of locations around the EC-station (one in each cardinal direction, Fig. 1) at the beginning of every observation period. In order to obtain an undisturbed soil monolith for each microlysimeter, an SDR-35 polyvinyl chloride (PVC) collar with an inner diameter of 0.2 m, a wall thickness of 0.05 m, and a depth of 0.11 m was pushed carefully into the ground. Afterwards the collar including the soil column was retrieved, its outside was cleaned, and the bottom of each lysimeter was sealed with an acrylic glass disc, which prevented percolation and capillary rise from or into the microlysimeter. The microlysimeters were then weighed



initially and returned to their original positions. We made sure that the lysimeters were levelled with the soil surface, their walls fully surrounded by soil, and the that crop was affected and destroyed as little as possible, so that the general conditions and characteristics of the field site could still be maintained (e.g., regarding heat flux, shading). Subsequently, all four microlysimeters were collected, cleaned, weighed, and distributed again every 60 or 90 minutes. A scale with a precision of 0.1 g (equivalent to 0.00318 mm<sup>2</sup> evaporation) was used, which had to be enclosed in a box to avoid wind effects. Finally, the measured weight differences were converted to W m<sup>-2</sup> by means of the lysimeters surface area, the time periods between weighing, and the latent heat of vaporization (Quade, et al., 2019).

### 2.3.2 Soil CO<sub>2</sub> flux chambers

Soil respiration ( $R_s$ ) was observed with an automated soil CO<sub>2</sub> gas flux system (Li-8100, Li-Cor Inc. Biosciences, Lincoln, Nebraska, USA), connected to four long-term soil flux chambers. The chambers were installed close to the EC-station (one in each cardinal direction, Fig. 1) on top of PVC soil collars with a diameter of 0.2 m and a total height of 0.07 m, from which 0.05 m was inserted into the soil. For flux measurement, each chamber was closed at 30-minute intervals for 90 seconds, while CO<sub>2</sub> and water vapour concentrations as well as chamber headspace temperature were recorded at a sampling rate of 1 Hz. The CO<sub>2</sub> concentration was corrected for changes in air density and water vapour dilution. Subsequently,  $R_s$  was calculated by adjusting only the final 60 seconds of the measurement before reopening against the corrected CO<sub>2</sub> concentrations by linear regression.

### 2.3.3 Leaf-level measurements

Leaf gas exchange was measured using a Li-Cor LI-6400XT portable photosynthesis system with a 6400-02B LED light source. Leaf-level measurements included instantaneous stomatal conductance to water vapour ( $g_{sw}$ ) and photosynthesis ( $A_{leaf}$ ), maximum light-saturated photosynthesis ( $A_{max}$ ), CO<sub>2</sub>-response curves, and light-response curves. Measurements of  $g_{sw}$  and  $A_{leaf}$  were performed during the three IOPs, starting at sunrise and ending when measurements of  $g_{sw}$  indicated that stomata had nearly closed ( $g_{sw} < 0.05$  mol m<sup>-2</sup> s<sup>-1</sup>). For measurements of  $g_{sw}$  and  $A_{leaf}$ , tillers were picked randomly from the field and immediately mounted in the leaf chamber for measurements. Initial tests showed no difference in  $g_{sw}$  between excised and attached tillers. Settings of leaf chamber PAR and CO<sub>2</sub> followed the diurnal variability measured in the field. For comparison with other observations, measurements of  $g_{sw}$  and  $A_{leaf}$  were binned and averaged at 30-minute intervals. Maximum light-saturated photosynthetic capacity ( $A_{max}$ ) was measured during the three IOPs as well as on 8<sup>th</sup> May between 10:00 and 12:00 UTC. For measurements of  $A_{max}$  the light intensity (PAR) was set to 1500 μmol m<sup>-2</sup> s<sup>-1</sup> and the leaf was equilibrated under a reference CO<sub>2</sub> concentration of 450 ppm. CO<sub>2</sub> response curves were measured during IOP 1 and IOP 3 prescribing CO<sub>2</sub> concentrations in the following order: 450, 50, 100, 150, 250, 350, 450, 600, 800, 1200 ppm. All CO<sub>2</sub>-response curves were measured using a light intensity (PAR) of 1500 μmol m<sup>-2</sup> s<sup>-1</sup>. Light response curves were measured on IOP 1 only and used a reference CO<sub>2</sub> concentration of 450 ppm. PAR values were changed in the following order: 0, 25, 50, 100, 200, 400, 800, 1200 1500 μmol m<sup>-2</sup> s<sup>-1</sup>. Leaves were allowed to equilibrate to leaf chamber conditions in terms of gas



exchange (approximately 1 to 2 minutes), but not in terms of stomatal aperture. For all measurements, leaf chamber temperature was controlled between 20°C and 25°C. Relative humidity in the leaf chamber was controlled between 60% and 75%. Measurements of  $A_{\max}$ , CO<sub>2</sub>-response curves and light-response curves were performed on attached tillers.

### 2.3.4 Sap-flow

5 Sap-flow in wheat tillers was measured with the heat-balance method (Sakuratani 1981; Baker and van Bavel, 1987). Twenty-four tillers were selected at random, diameters measured with an electronic calliper and SGA3-type sap-flow sensors installed at the lowest possible internodes following the procedure recommended by the manufacturer (Dynamax, 2007). Sensors were connected with electrically shielded wired to AM 16/32 multiplexers controlled and scanned by CR1000 data  
10 loggers (Campbell Scientific, Logan, Utah, USA). Energy supply to the stem heaters was carefully regulated to the highest possible level in order to obtain a strong heat signal. We employed the dual voltage regulators (Dynamax AVRDC) which were parts of wired measurement, control and extension units assembled and tested by the heat-balance sensor manufacturer (Flow32 1K A and B models, Dynamax Inc., Houston, Texas USA) Data were processed according to the calculation procedure of Dynamax (2007) with adaptations to wheat (Langensiepen et al. 2014) to obtain reliable data on the convective heat flow generated by sap flow. Here we take the evolution of the tiller densities from 480 tillers m<sup>-2</sup> (IOP 1 and IOP 2) to  
15 370 tillers m<sup>-2</sup> (IOP 3) into account.

### 2.3.5 Profiling-elevator

Vertical profiles of carbon dioxide (CO<sub>2</sub>) and water vapour (H<sub>2</sub>O) expressed as mole fractions  $\chi_{CO_2}$  and  $\chi_{H_2O}$  (mole of substance per mole of moist air), temperature ( $T_{air,p}$ ) and wind speed ( $u_p$ ) from the soil surface to the surface layer above the crop canopy were measured with a portable elevator system. The elevator continuously moved up and down the measuring  
20 sensors attached to an extension arm over a total profile height of 2 m. A sampling tube connected to a differential gas analyser (LI-7000, Li-Cor Inc. Biosciences, Lincoln, Nebraska, USA) collected  $\chi_{CO_2}$  and  $\chi_{H_2O}$  at a frequency of 20 Hz.  $T_{air,p}$  and  $u_p$  were measured at the same frequency by a ventilated fine wire thermocouple (FW3, Campbell Scientific, Logan, Utah, USA) and a hotwire anemometer (8455-075-1, TSI, Shoreview, Minnesota, USA) . All measurements were duplicated as a continuous fixed-height measurement at the top of the profile. During the data post-processing, the temporal and vertical  
25 resolution of the mean profiles was set to a time-averaging block of 30 minutes with a vertical resolution of 0.025 m. Time delays in each variable with respect to the position caused by response times of the sensors, electronic delays and the tube transport of the gas samples were adjusted by a hysteresis minimization algorithm. Detailed information on the profile measurement setup and the processing the data profile is given in Ney & Graf (2018). The measured concentration profiles were then used to determine the vertical source profiles of CO<sub>2</sub> and H<sub>2</sub>O, with the aim of providing an independent, non-  
30 invasive partitioning between aboveground net primary production (NPP) and R<sub>s</sub> or evaporation ( $E$ ) and transpiration ( $T$ ). To estimate source profiles and flux partitioning we used an analytical dispersion Lagrangian technique introduced by Warland



& Thurtell (2000) and further developed by Santos, et al. (2011). Other than in the abovementioned literature, a simple optimization method (Nelder & Mead, 1965) was used to fit four parameters: soil source, canopy source and shape parameters  $p$  and  $q$  of a beta distribution which describes the vertical source distribution within the canopy.

### 2.3.6 Scintillometer

5 A displaced-beam laser scintillometer, hereafter referred to as DBLS (SLS-20, Scintec, Rottenburg, Germany), was placed 9 m south-east from the EC station (Fig. 1). The scintillometer measurements height was 1.95 m a. g. l.. The path length was 86.8 m and was directed North-West to South-East. The DBLS measures the scintillation intensity of two displaced laser-beams (wavelength of 670nm and separation distance of  $\sim 2.7$ mm). From the log-variance of one beam and log-covariance between the beams, the structure parameter of temperature,  $C_T^2$  and dissipation rate of turbulent kinetic energy,  $\varepsilon$ , are  
10 determined. The general equation that links the scintillometer measurements to fluxes is given by:

$$F_x = \rho K_x \left( u_*, \frac{z}{L} \right) z^{\frac{1}{3}} \sqrt{C_x^2} \quad (2)$$

where  $F_x$  is defined as the turbulent flux,  $C_x^2$ , is the structure function of the transported variable  $x$ ,  $K_x$  represents the turbulent exchange coefficient that links  $F_x$  to  $C_x^2$ , which is a function of the friction velocity,  $u_*$  and the Monin-Obukhov  
15 length,  $L$  and finally  $\rho$  is the air density and  $z$  the measurement height above the surface. For the sensible heat flux,  $H$ ,  $x$  is given by  $T$  whereas for the fluxes of  $H_2O$  and  $CO_2$   $x$  represents the specific density,  $q_x$  of  $H_2O$  or  $CO_2$ .  $H$ ,  $u_*$  and  $L$  are solved iteratively as a function of the DBLS measured  $C_T^2$  and  $\varepsilon$ . Appropriate constants need to be added to convert Eq. (2) to energy fluxes. The Monin-Obukhov Similarity Theory (MOST) functions that define  $K_x$  were taken from Kooijmans and Hartogensis (2015). For our purpose, however, the exact shape of the MOST functions that mainly defines the size of the  
20 fluxes is of minor importance as we are primarily interested in the dynamic, temporal behaviour of the fluxes rather than an accurate description of their quantitative values.

These, in turn, are related to the sensible heat flux,  $H$ , and friction velocity,  $u_*$ , following Monin-Obukhov similarity theory (Thiermann, 1992; Hartogensis et al., 2002). The added value of DBLS fluxes over the traditional EC method is that they converge to statistically stable flux estimates at much shorter flux averaging times of 1 minute or less, while the EC  
25 technique typically requires flux averaging times of 10 to 30-minutes (Hartogensis et al, 2002; van Kesteren et al., 2013b). We also adopted the combination technique introduced by van Kesteren et al. (2013a, 2013b) to obtain fluxes of  $H_2O$  and  $CO_2$  at these fine time scales. This technique combines structure parameters of  $H_2O$  and  $CO_2$  which are obtained from  $H_2O$  and  $CO_2$  time-series from an Infra-Red Gas Analyser (IRGASON system; see second eddy-covariance description in Sect. 2.3.7) with an exchange coefficient defined by the DBLS fluxes to finally calculate flux estimates of  $H_2O$  and  $CO_2$ .

30



### 2.3.7 Eddy-covariance and ancillary micrometeorological measurements

A continuously running EC system was operated in the middle of the field (Fig. 1), comprising a three-dimensional sonic anemometer (Model CSAT-3, Campbell Scientific, Inc., Logan, Utah, USA) and an open path infrared gas analyser (Model LI-7500, Li-Cor, Inc., Biosciences, Lincoln, Nebraska, USA). The sensors height was 2.5 m a. g. l. Raw data were sampled in 20 Hz mode and fluxes and averages were calculated as 30-minutes block averages using the TK3.11 software package from the University Bayreuth, including corrections and quality control as given in Mauder, et al. (2013). Missing values in the calculated turbulent fluxes were filled with the marginal distribution sampling (MDS) method after Reichstein, et al., (2005) which is implemented in the REddyProc software package (REddyProc Wutzler et al., 2018). The station also included measurements of all components of the radiation budget (NR01, Hukseflux, Delft, the Netherlands), photosynthetically active radiation or PAR (LI-190R, Li-Cor Inc. Biosciences, Lincoln, Nebraska, USA and BF5, Delta-T Devices, Cambridge UK), air temperature ( $T_{\text{air}}$ ) and humidity (HMP45C, Vaisala Inc., Helsinki, Finland) at 2.105 m, and precipitation (Thies Clima type tipping bucket, distributed by Ecotech, Bonn, Germany) at 1.0 m a. g. l. Soil heat flux, temperature, moisture were measured next to the station (3 x HFP01SC at 3 and 8 cm, Hukseflux, the Netherlands, 3 x TCAV, Campbell Scientific, Logan, USA, 1 cm, 5 cm and 2 to 65 cm layer average, 2 x CS616, Campbell Scientific, Logan, USA, 2 to 6 cm layer average), but also at five points distributed across the field using the wireless SoilNet sensor system (Bogena, et al., 2010). One SoilNet point was placed next to the station, while the other four were placed next to the soil CO<sub>2</sub> efflux chambers described above. Each SoilNet point comprised a single soil heat flux measurement at 5 cm (HFP01SC, see above) and combined temperature and soil water content measurements in depths of 1, 5, 10, 20, 50 and 100 cm (SMT100, Truebner GmbH, Neustadt, Germany).

A second mobile EC station at a height of 1.93 m a.g.l. was deployed in the immediate vicinity of the continuously running station during the measurement campaign. The system comprised an IRGASON EC system (SN1185 Irgason EC150, Campbell Scientific, Inc., Logan, Utah, USA; PTB101B pressure sensor, Vaisala Inc., Helsinki, Finland) with an additional LI-7500 sensor (same manufacturer). Here, fluxes were processed with the LiCor EddyPro v6.2.2 software. Radiation (CM11 for global and CG2 for long wave radiation, Kipp & Zonen B.V., Delft, Netherlands ), ground heat flux (4 x HFP01SC at 5 cm depth, Hukseflux, the Netherlands) and temperatures at depths of 2 cm (4 x) and 8 cm (2 x) were also measured at this station.

### 2.3.8 Canopy-level measurements of reflectance and sun-induced fluorescence (SIF): FloxBox

For canopy-level measurements of reflectance and SIF, a field spectroscopy system was used (FLOX, JB Hyperspectral Devices UG, Düsseldorf, Germany). FLOX is constructed for high temporal frequency acquisition of continuous top-of-canopy optical properties with a focus on sun-induced chlorophyll fluorescence. The system is equipped with two spectrometers: an Ocean Optics FLAME S, covering the full range of Visible and Near-Infrared (VIS-NIR) and an Ocean Optics QEPro, with high spectral resolution (Full Width at Half Maximum – FWHM - of 0.3 nm) in the 650-800 nm range of



the fluorescence emission. The optical input of each spectrometer is split between two fibre optic cables, that lead to a cosine receptor that measures solar irradiance and a bare fibre bundle that measures the target-reflected radiance. Spectrometers are housed in a Peltier thermally regulated box in order to keep the internal temperature lower than 25 °C in order to reduce dark current drift. The signal is automatically optimized for each channel at the beginning of each measurement cycle and two associated dark spectra are collected as well. Metadata such as spectrometer temperature, detector temperature and humidity, Global Positioning System (GPS) coordinates and time are also stored in the secure digital memory of the system. More detailed information about the system can be found in Wohlfahrt (2018) and in Campbell (2019).

### 2.3.9 Regional level measurements of reflectance and sun-induced fluorescence (SIF):HyPlant

For regional level measurements of the same quantities, the airborne high performance imaging spectrometer (HyPlant) was used, several flight lines over the 15 km x 15 km study site with 1-3 m pixel resolution. HyPlant is a hyperspectral imaging system for airborne and ground-based use, developed as a cooperative effort between Forschungszentrum Jülich (Germany) and the company SPECIM (Oulu, Finland). It consists of two sensor heads, named DUAL and FLUO. The DUAL module is a line-imaging push-broom hyperspectral sensor, which provides contiguous spectral information from 370 nm to 2500 nm in a single device that utilizes a standard objective lens with 3 nm spectral resolution in the VIS/NIR spectral range and 10-nm spectral resolution in the SWIR spectral range. The FLUO module measures the vegetation fluorescence signal with a separate push-broom sensor which produces data at high spectral resolution (0.25 nm) in the spectral window between 670 and 780 nm. The Position and Altitude Sensor (GPS/INS sensor) provides, synchronously with the image data, aircraft position and altitude for image rectification and geo-referencing. Both imagers are mounted in a single platform with the mechanical capability to align the field of view (FOV). A more detailed description of the sensor is given in Rascher, et al. (2015).

Sun-induced fluorescence ( $F_{687}$  and  $F_{760}$ ) was retrieved in the two oxygen absorption bands according to the iFLD method, surface reflectance and vegetation indices was calculated after an atmospheric correction using the MODTRAN software package was applied (for an overview of the data processing of HyPlant see Siegmann et al. 2019). For the reasons of easier comparison of SIF values with other methods of this paper, the commonly used SIF units ( $\text{mW m}^{-2} \text{sr}^{-1} \text{nm}^{-1}$ ) were replaced by  $\text{nmol m}^{-2} \text{sr}^{-1} \text{s}^{-1}$  using conversion the factors 6.35 for  $F_{760}$  and 5.74 for  $F_{687}$ .

### 2.3.10 Boundary-layer and cloud remote sensing measurements

JOYCE remote sensing facility (Löhnert, et al., 2015) (located at a distance of 5 km from the test site) provided continuous information on the boundary-layer and cloud characteristics. Specifically, the microwave and LIDAR were used to compare the CLASS model results (see next section) with the inferred boundary-layer depth. This comparison was completed by vertical profiles measured by the routine radio soundings at Essen (station ID EDZE/10410 at a distance of 75 km).



## 2.4 Modelling from leaf to landscape scales: CLASS

The Chemistry Land-surface Atmosphere Soil Slab (CLASS, <https://classmodel.github.io/>) is a model that couples the soil-vegetation-atmospheric processes and is used to interpret the observations and analyse the interaction of scales (Vilà-Guerau de Arellano, et al., 2015). It contains a leaf-level representation of photosynthesis and stomatal aperture (leaf resistance). By upscaling this leaf resistance to the canopy level (surface canopy resistance), it connects with the soil and surface and boundary-layer diurnal dynamics. In 2.4.1 and 2.4.2 we will subsequently discuss the two main modules of CLASS that we will target in this paper, i.e. the leaf level photosynthesis module and the mixed layer module.

### 2.4.1 Modelling leaf-level photosynthesis

Leaf-level photosynthesis was modelled using the representation of photosynthetic biochemistry, as included in CLASS (Vilà-Guerau de Arellano, et al., 2015), which was originally developed by Goudriaan (1986) and further adapted to meteorological applications by Jacobs & de Bruin (1997). As this model describes the relationship between stomatal conductance ( $g_s$ ) and photosynthesis ( $A$ ), it is usually referred to as the A- $g_s$  (sub)model. In short, plant transpiration and CO<sub>2</sub> assimilation as part of the surface energy balance model are represented by a two-big leaves model, one for sunlit leaves and one for shaded leaves (Jacobs & de Bruin, 1997; Pedruzo-Bagazgoitia et al., 2017). The exchange at the leaf surface depends on the gradient of atmospheric CO<sub>2</sub> and an internal leaf CO<sub>2</sub> concentration which depends on the water-vapour deficit, and leaf conductance. The CO<sub>2</sub> exchange is upscaled to the canopy level by integrating over the leaf area index (LAI).

In setting up the model we made ample use of the available field measurements. The parameters representing the initial value of the light-use efficiency ( $\alpha_0$ ) and the temperature-normalized maximum leaf-level photosynthesis rate ( $A_{m,max298}$ ) were fitted using light-response curves (Fig. 5a), and CO<sub>2</sub>-response curves (Fig. 3b) collected on 8<sup>th</sup> May 2018 (one day after IOP 1), respectively. Table 3 summarizes the optimized values used in the A- $g_s$  (sub)model. The A-PAR curves contain only the lower light intensity values (0-200  $\mu\text{mol m}^{-2} \text{s}^{-1}$ ) for which the light response is near-linear and not limited by CO<sub>2</sub> diffusion into the leaf. As leaf-level measurements of  $A_{max}$  indicated a decline in photosynthetic capacity in the course of the growing season (Fig. 5c), we performed additional measurements of  $A_{m,max298}$  to represent the observed seasonal decline for IOP 2 and IOP 3. Fitted parameter values used to simulate leaf-level photosynthesis rates are shown in Table 1.

### 2.4.2 Modelling the diurnal variability of landscape surface fluxes and boundary-layer dynamics

The fundamental assumption of the mixed-layer model is that under convective conditions the atmospheric boundary layer (ABL) dynamics lead to profiles of the meteorological state variables that are uniform (well-mixed) with height. As a result, these state variables are governed by horizontally averaged 0-dimensional slab equations: one equation for the evolution through time of the slab variable and another for the difference between the residual layer (in the morning transition) and the free tropospheric values and the slab value, i.e. the jump at the interface between residual layer and ABL. The ABL dynamics are governed by the mixed-layer equations of potential temperature (heat), specific humidity (moisture), CO<sub>2</sub> and



the two horizontal wind components (momentum). In addition, there is an equation that governs the boundary-layer growth which depends on the buoyancy flux at the surface and the jump in the virtual potential temperature at the interface between the atmospheric boundary layer and the free troposphere.

A key feature of the model is its representation of the sub-daily variability of the land-atmosphere interactions (van Heerwaarden, et al., 2010; Vilà-Guerau de Arellano, et al., 2015). The net ecosystem exchange is calculated as a result of the assimilation of CO<sub>2</sub> by plants and the CO<sub>2</sub> soil efflux. We calculate the assimilation rate from photosynthesis and the stomatal aperture measurements at leaf level (see previous section), up-scaled to canopy level (Ronda, et al., 2001). This model depends on the diurnal variability of PAR, temperature ( $T_{air}$  and  $T_{air,p}$ ) and the water-vapour deficit (VPD). The two-big leaves approach is used (sunlit and shaded) to take the different contributions of direct and diffuse radiation into account (Pedruzo-Bagazgoitia, 2017). The soil efflux is calculated as a function of the soil temperature and moisture. Other relevant physical processes include a radiation transfer model, the Penman-Monteith equation included in the surface energy balance, and the possibility of adding large-scale forcings such as vertical subsidence motions and large-scale advection of momentum, heat, moisture and CO<sub>2</sub>. Within the context of CloudRoots, it is important to mention that the model assumes a horizontal homogeneous surface. While the experimental field itself is quite homogeneous, it is surrounded by other land-use types at a spatial scale that will affect the boundary layer. In that respect, and in setting the initial and boundary conditions for the numerical case, we assume that the boundary layer dynamic is governed by a sensible heat flux that is an aggregate of all the fields shown in Fig. 1.

### 3 Results: Integrating spatiotemporal scales from leaf to boundary layer

This section is structured following the five facets of the diurnal interactions between the land and the atmosphere outlined in the introduction.

#### 3.1 Leaf-level exchange of CO<sub>2</sub> and H<sub>2</sub>O: observations and modelling

We combine leaf-level and sap flow measurements of tiller assimilation and transpiration with leaf-level assimilation modelled by CLASS, A-g<sub>s</sub> representation, to study their variation during the growing season and the impact of unsteady PAR due to the presence of clouds.

##### 3.1.1 Stomatal conductance and sap flow

Our leaf-level measurements revealed clear diurnal patterns in  $g_{sw}$  during all the IOPs (Fig. 3). The observed daily maximum  $g_{sw}$  fell over the growing season and the maximum  $g_{sw}$  occurred at an earlier time during each IOP. Specifically, the 30-minute average daily maximum  $g_{sw}$  declined from 0.84 mol m<sup>-2</sup> s<sup>-1</sup> during IOP 1 and 0.83 mol m<sup>-2</sup> s<sup>-1</sup> during IOP 2 to 0.30 mol m<sup>-2</sup> s<sup>-1</sup> during IOP 3. The daily maximum  $g_{sw}$  was attained between approximately 10:00 and 14:00 UTC in IOP 1 between 8:00 and 11:00 UTC during IOP 2, and between 5:00 and 7:00 UTC during IOP 3. The weather during IOP 2 was



characterized by large cumulus clouds passing over the field site, which were made visible in the large fluctuations in PAR (Fig. 3b, 11 and 12). The cloud-induced changes in light intensity induced consistent stomatal opening-closing responses during IOP 2. Interestingly, the increased light intensity induced stomatal opening responses until approximately 12:00 UTC, whereas the opposite response was observed later during the day. The relatively low  $g_{sw}$  observed during IOP 3 probably reflects the continuing drought that characterized the 2018 growing season in combination with the relatively high VPD and high temperatures. Sap flow measurements were performed during IOP 2 and IOP 3 (Fig. 5b, c), and one earlier non-IOP day (7<sup>th</sup> June) (Fig. 4). Measurements of sap flow revealed clear diurnal patterns for all measurement days and consistent responses to cloud-induced changes in light intensity during IOP 2. These responses were comparable to the observed responses in  $g_{sw}$  during IOP 2. Interestingly, the notable decline in leaf-level  $g_{sw}$  between IOP 2 and IOP 3 was not reflected in the measurements of sap flow. This discrepancy could partly be explained by the increase in VPD and wind speed between IOP 2 and IOP 3. The more probable causes are senescence effects on physiological control of transpiration and the physical reactions to heat of the wheat tillers which were noticeably wilting between IOP 2 and IOP 3. This observation has not been so far reported in the literature. Further study of the relationship between senescence and simultaneously occurring changes in the heat-physical properties of wheat tillers is needed to explain this phenomenon.

### 3.1.2 Observed versus modelled leaf-level photosynthesis

A main aim in CloudRoots is to improve the mechanistic modelling of photosynthesis and stomatal aperture. To this end, we calibrate the constants of the A-g<sub>s</sub> model using systematic in-situ field observations. Fig. 5 shows the dependencies of leaf-level photosynthesis on PAR (Fig. 5a) and the leaf-internal concentration (Fig. 5b), and the long-term decline in maximum light-saturated photosynthesis (Fig. 5c). Table 2 summarises the new constant values used in the A-g<sub>s</sub> model. Our observations indicate the need to calibrate the model depending on the functional type of the plant, in particular the dependence of  $A_{leaf}$  on PAR

Fig. 6 shows a comparison of the model results of  $A_{leaf}$  using the new constants and the measurements of  $A_{leaf}$  and NPP together with the diurnal variation in PAR and VPD during the three IOPs. Our measurements and model results of  $A_{leaf}$  showed clear diurnal patterns during each IOP, and a consistent decline over the three IOPs. The decline in  $A_{leaf}$  was comparable to the decline in  $A_{max}$  (Fig. 3c) and probably reflects a combination of seasonal decay in photosynthetic capacity and increasing stomatal limitations owing to persistent drought, especially during IOP 3. The magnitude of the seasonal decline in  $A_{leaf}$  was comparable to the seasonal decline in NPP derived from EC data. Cloud-induced changes in PAR during IOP 2 also induced changes in  $A_{leaf}$ . The A-g<sub>s</sub> model reproduced the diurnal patterns in  $A_{leaf}$  during each IOP as well as the cloud-induced changes in  $A_{leaf}$  during IOP 2. The agreement is very satisfactory during IOP 1 characterized by cloudless conditions and the maturity of winter wheat. The model underestimated  $A_{leaf}$  during IOP 3, which was a result of the strong stomatal limitations that influenced the measurement of  $A_{max}$  on which the model parameterisation from IOP 3 was based. The model furthermore underestimates the decline in  $A_{leaf}$  between 15:00 and 19:00 UTC, which probably reflects a misrepresentation of the temperature and VPD sensitivity of *Triticum aestivum*.



### 3.2 Canopy-level partitioning of the net H<sub>2</sub>O and CO<sub>2</sub> fluxes between soil and plant processes

Moving from leaf to canopy scale, we analyse the detailed profiles of micrometeorology and carbon dioxide collected using the elevator and infer vertical assimilation profiles as well as the diurnal variability in the surface contributions to ET and NEE.

#### 5 3.2.1 Concentration profiles of H<sub>2</sub>O and CO<sub>2</sub>, temperature and wind speed

Fig. 7 shows selected 30-minutes mean profiles of  $\chi_{CO_2}$  and  $\chi_{H_2O}$ , temperature and wind speed versus height (z) above ground level (a.g.l.) during IOP 1 and IOP 2. Over the diurnal cycle,  $\chi_{CO_2}$  concentrations fell between 0800 and 1300 UTC from 370 to 360  $\mu\text{mol mol}^{-1}$  in the mid canopy during IOP 1 but stagnated slightly below 370  $\mu\text{mol mol}^{-1}$  during IOP 2. This seasonal reduction in CO<sub>2</sub> uptake was also observed in measured  $A_{leaf}$  (Fig. 6). The lowest values were observed during local noon, simultaneously with the highest PAR values (Fig. 5b).  $\chi_{CO_2}$  minima were located in the upper third of the canopy during IOP 1 and during the middle third during IOP 2. The highest  $\chi_{CO_2}$  values were found near the soil surface due to soil respiration, lower light intensity caused by shadowing and a low amount of photosynthetic organs in the stems. Maximum  $\chi_{CO_2}$  concentrations were measured in the morning and evening hours and peaked at about 475 and 420  $\mu\text{mol mol}^{-1}$  during IOP 1 and IOP 2, respectively. The photosynthetic CO<sub>2</sub> uptake by plants is highly related to plant transpiration. Consequently,  $\chi_{H_2O}$  in the canopy space was higher than in the air above the canopy. The highest values were found directly above the soil surface and were caused evaporation, and within the canopy due to plant transpiration.

The highest temperatures appeared near the canopy top (Fig. 7d, 6e, 7j and 7l). In the late morning of IOP 2, the temperature reached a distinct maximum just below the canopy top (Fig. 7j). This phenomenon has been reported in previous studies (Ney and Graf, 2018) and is caused by the changing solar incidence angle. A low angle of incidence in the morning and afternoon limited the heating to an area just below the canopy surface. Previous studies have shown that the presence or absence of such a pronounced temperature maximum has the potential to increase thermal stability within the canopy and thus inhibit the vertical turbulent exchange of sensible heat (Gryning, et al., 2001; Ney & Graf, 2018, Sikma et al., 2020). It can be assumed that the sensible heat flux within the dense plant stand was largely determined by the entire canopy. In other words, during the day, mixing near the soil surface was impeded by stable temperature stratification while in the evening, cooling expanded upwards from the soil surface (Fig. 7f). In general, the processes described above were more pronounced during IOP 2 with its greater canopy height than with the lower canopy during IOP 1. The vertical wind profile showed consistently low wind speeds within the dense canopy ( $< 0.5 \text{ m s}^{-1}$ ). Above the canopy layer, the wind speed increased in a log-like profile up to a maximum of  $2 \text{ m s}^{-1}$ .



### 3.2.2 Profiles of gross primary production

The detailed profile observations presented in the previous section enable us to calculate height resolved estimates of gross primary production  $A$ . Using the 30 min-averages of the vertical profiles for temperature, moisture, and CO<sub>2</sub> in the canopy,  $A$  is determined using the A-g<sub>s</sub> model (Jacobs et al., 1997; Ronda et al., 2001).  $A$  (mg m<sup>-3</sup> s<sup>-1</sup>) is calculated as follows:

5

$$A = LAD (A_m(h) + R_d(h)) \left[ 1 - \exp\left(\frac{-\alpha PAR(h)}{A_m(h) + R_d(h)}\right) \right] \quad (1)$$

where LAD (m<sub>leaf</sub><sup>2</sup> m<sup>-3</sup>) is the leaf area density,  $A_m(h)$  is the CO<sub>2</sub> primary productivity (mg m<sub>leaf</sub><sup>2</sup> s<sup>-1</sup>) as a function of height  $h$ ,  $R_d(h)$  (mg m<sub>leaf</sub><sup>2</sup> s<sup>-1</sup>) the CO<sub>2</sub> dark respiration as a function of  $h$ ,  $\alpha$  (mg J<sup>-1</sup>) the light use efficiency, PAR( $h$ ) (W m<sup>-2</sup>) the amount of available photosynthetically active radiation within the canopy. Solar zenith angle induced variation in PAR intrusion and differences between atmospheric and skin values for temperature, moisture, and CO<sub>2</sub> are neglected. Fig. 8a shows the winter wheat LAD applied in the calculation.

Fig. 8b shows that the entire canopy contributes to the photosynthetic activity, but with maximum  $A$  at  $h/h_c = 0.7$ . This is primarily caused by the extinction of PAR within the canopy and reduced leaf density distribution close to the ground (Fig. 8a). Maximum productivity is found at around  $h/h_c = 0.7$ , with the diurnal maximum at 12:00 UTC. Integration over the canopy shows minor discrepancies with respect to the bulk A-g<sub>s</sub> model calculation, as the profile data allows for a more precise evaluation of photosynthetic activity. The profile approach therefore allows for an improved modelling of the photosynthetic CO<sub>2</sub> uptake of vegetation depending on height, and more accurate estimates of CO<sub>2</sub> gross primary production.

15

### 3.2.3 Profile based partitioning of CO<sub>2</sub> and H<sub>2</sub>O

Fig. 9 shows the measured fluxes of latent heat, NEE and soil respiration, as well as their partitioning based on the inversion of vertical high-resolution concentration profiles into the evaporation/transpiration and R<sub>s</sub>/NPP components. In this section, positive values indicate a flux from the surface/plants into the atmosphere and vice versa. During IOP 1, measured latent heat flux ( $L_v E$ , hereafter referred to as  $ET_{ec}$ ) showed a typical daily pattern under clear sky conditions (Fig. 9a) with maximum  $ET_{ec}$  at noon (345 W m<sup>-2</sup>). Using both methods, evaporation  $E$  of both methods displayed comparable values in the morning and evening but differed at midday. In the morning,  $E_p$  and  $E_{lysi}$  both consistently suggested low  $E/ET$  fractions with  $E$  below 10 W m<sup>-2</sup>. Towards noon,  $E_p$  increased to 25 and  $E_{lysi}$  to 60 W m<sup>-2</sup>, and in the afternoon  $E_{lysi}$  reached a maximum of 101 ± 41 W m<sup>-2</sup> (no  $E_p$  available). Estimated  $T_p$  increased to about 290 Wm<sup>-2</sup> at 11:00 UTC, this being the highest diurnal proportion of  $ET$ . Lower  $T_p$  levels around 1200 UTC are probably due to a sub-optimal performance of the profile-based partitioning.

25

Variations in CO<sub>2</sub> fluxes NEE, NPP and R<sub>s</sub> during IOP 1 are shown in Fig.9b. NEE<sub>ec</sub> followed a typical diurnal cycle, with strong negative fluxes during the day and slightly positive values (carbon source) during transition times. The highest NEE

30



was observed before noon ( $-25 \mu\text{mol m}^{-2} \text{s}^{-1}$ ).  $\text{NPP}_p$  followed the graph of  $\text{NEE}_{ec}$ , with higher values ( $-26 \mu\text{mol m}^{-2} \text{s}^{-1}$ ) in the morning hours than during the afternoon under comparable PAR values. This behaviour coincides with the photosynthesis rate observed at leaf level in Fig. 6a and provides further evidence that carbon uptake by plants was limited due to stomatal occlusion caused by the increase in VPD (Fig. 6a) and/or  $T_{air}$  in the afternoon. Profile-based  $R_{s,p}$  ranged between 0.5 to 6  $\mu\text{mol m}^{-2} \text{s}^{-1}$  with higher values around noon. Compared to measured  $R_{s,ch}$ ,  $R_{s,p}$  lay within the standard deviations of  $R_{s,ch}$ , though  $R_{s,p}$  was significantly lower during the morning and evening hours.

### 3.3 Effects of clouds on surface turbulent fluxes

#### 3.3.1 Cloud-induced diffuse fertilization effect on evapotranspiration

Clouds affect plant photosynthesis by increasing the fraction of diffuse solar radiation that arrives at the top of the canopy (Kanniah, et al., 2012). With a larger contribution of diffuse solar radiation, and within the canopy, the radiation spreads more equally over all leaves and thereby increasing the light-use efficiency of a canopy (Farquhar & Roderick, 2003). At a constant level of radiation at the top of the canopy, the increased light-use efficiency results in enhanced canopy photosynthesis which is known as the diffuse fertilization effect (Roderick, et al., 2001). This phenomenon is especially noticeable for canopies with a high LAI (Knobl & Baldocchi, 2008; Dengel & Grace, 2010). In CloudRoots, and due to the high values of LAI (values in between 4.5 to 5.5), we expect situations in which diffuse fertilisation occurs, but here the question is how it influences  $L_vE$ . Previous modelling studies by Pedruzo-Bagazgoitia, et al. (2017) have shown that under conditions dominated by clouds with a small optical depth, *i.e.* thin clouds,  $L_vE$  is enhanced with respect to its clear-sky values at the same radiation level. We use a two-week period of observations, between 7<sup>th</sup> May and 20<sup>th</sup> May 2018, to analyse whether a higher diffuse fraction also leads to an enhancement of the latent heat flux. As  $L_vE$  is mainly driven by net radiation ( $Q^*$ ), in Fig. 10 we compare  $L_vE$  under clear and cloudy skies at a constant level of  $Q^*$  at the top of the canopy.

We find that the observed  $L_vE$  is higher, rather than lower, during clear conditions (less diffuse light) than to the more diffused cloudy conditions. At constant  $Q^*$ , the median of  $L_vE$  is always higher under clear skies than for cloudy skies. Diffuse fraction plays a minor role and the decrease on  $L_vE$  under cloudy conditions is mainly due to the reduction in the incoming shortwave radiation. Our observations point toward the idea that  $L_vE$  is driven by the partitioning of direct and diffuse radiation, but also other effects such as diurnal variations of temperature and the link to VPD may partially compensate for the different distribution of direct and diffuse radiation caused by clouds. For both clear and cloudy skies, the shaded area below the median represents conditions before 1130 UTC and the shaded area above the median represents conditions after 1130 UTC, *i.e.* implying a hysteresis loop (Zhang et al., 2014). This spread in  $L_vE$  at a constant level of  $Q^*$  is caused by a difference in VPD between morning (before 1130 UTC) and afternoon (after 1130 UTC). This is because on a clear day the VPD raised rapidly due to its non-linear dependence on temperature relative to a cloudy day. In a typical clear day at CloudRoots, the value of  $200 \text{ W m}^{-2}$  for  $Q^*$  is crossed twice: once in the morning and once in the afternoon. When  $200 \text{ W m}^{-2}$  is crossed in the morning, the VPD is around 1000 Pa and reaches a value of 2000 Pa in the afternoon. On the other



hand, on a cloudy day with similar values of around  $200 \text{ W m}^{-2}$  the VPD remains almost constant through the entire day and with a value of  $1000 \text{ Pa}$  at 11:30 UTC. The higher VPD values during the day partly offset the more optimal PAR conditions and therefore cause a closing of the stomatal that leads to decreases in  $L_vE$ .

The influence of VPD on  $L_vE$  also has the effect that the diurnal cycles of  $Q^*$  and  $L_vE$  are out of phase due to the fact that  $L_vE$  depends on the leaf temperature.  $Q^*$  is primarily a function of incoming shortwave radiation and VPD of air temperature at the leaf surface. As a result,  $Q^*$  and VPD peak at different times of the day.  $Q^*$  peaks at maximum incoming shortwave radiation (local noon is at 11:30 UTC), and near-surface VPD times when air temperature peaks, which is around the time at which  $Q^* = 0$  (17:00UTC). The diurnal cycle of the sun implies there is a short period around 11:30 UTC when  $Q^*$  does not change. On the contrary, air temperature increases almost linearly around 11:30 UTC due to the approximately constant  $Q^*$ , as does VPD. Therefore, peak values for  $L_vE$  are found between the moment of maximum  $Q^*$  and the moment of maximum VPD. For this dataset, the peak of  $L_vE$  is around 1200 UTC for both clear and cloudy skies although the peak for cloudy skies is less distinct due to the more fluctuating daily cycle of  $Q^*$ . Because  $Q^*$  and  $L_vE$  are out of phase, the highest values for  $L_vE$  do not occur in the bin with the highest net radiation, but rather in the bin of  $400\text{-}500 \text{ W m}^{-2}$  (which roughly contains data from 11:00 UTC and after 12:00 UTC).

### 3.3.2 Cloud-induced radiation perturbations and response by turbulent fluxes

The short interval fluxes (1 min) of the double beam laser scintillometer (DBLS) technique enable us to study the vegetation response to rapid radiation perturbations due to changes in cloud cover. The goal here is to illustrate this potential by discussing selected time-series under changing cloud conditions during IOP 2. The morning of IOP 2 was characterized by rapidly changing cloud conditions due to the overpass of a shallow cumulus cloud deck. A breakdown of the 1min DBLS sensible heat flux in terms of contributions from turbulent exchange ( $K_T$ ) and the measure for temperature fluctuations ( $C_T^2$ ) is given in Fig. 11. This figure also depicts, on the same axes, scaled time-series of wind speed and PAR that can be regarded as proxies that fuel mechanically induced turbulence (wind speed) and buoyancy turbulence (radiation in general) as well as photosynthesis (PAR).

First of all, the 1min DBLS fluxes of  $H$  closely follow the cloud cover induced radiation changes, but with a time-lag of 45-120 seconds (Fig. 11a). This is similar to those reported by van Keesteren et al. (2013b).  $H$  fluxes measured with EC techniques even when estimated over the relatively short interval of 10 minutes, which is not a standard output, are not capable of capturing such rapid dynamic behaviour of the flux regime (Fig. 11a). The dynamic behaviour in the DBLS  $H$  is mainly governed by fluctuations in  $T$  expressed by  $C_T^2$  (Fig. 11c) and to a lesser extent is due to changes in the exchange coefficient  $K_T$  (Fig. 11b). Note that is impossible to fully distinguish the three variables  $H$ ,  $K_T$  and  $C_T^2$  from each other as they are all inter-connected, e.g.  $K_T$  is defined in terms of the Obukhov length  $L$ , which in turn depends on  $H$  and  $u^*$ . Nevertheless, our high-time-resolution observations demonstrate that changes in PAR induce very fast responses of the transported quantity  $T$  (Fig. 11c). Even in the absence of strong wind-induced variations in  $K_T$ , these  $T$  variations lead to



approximately similar dynamic behaviour of  $H$ . On top of this, the additional, but smaller wind induced fluctuations in  $K_T$  are also reflected in  $H$  and lead to “noise” in the variability of  $H$  compared to the cloud-induced on-off behaviour of PAR. Next we examine how soon the fluxes of  $H_2O$  and  $CO_2$  respond to the cloud induced radiation changes. Fig. 12 demonstrates that there is indeed a fast response, and the one-minute resolution fluxes of  $H_2O$  and  $CO_2$  allow us to precisely determine a delay time of approximately 2 minutes in the increases  $CO_2$  uptake and transpiration of  $H_2O$  relative to the changes in PAR. The delay is once again undetectable with the standard 30-minutes eddy-covariance results (Fig. 12). This behaviour is in line with what was concluded about the state of the vegetation observed at leaf level (Sec. 3.1). As the vegetation is not water-stressed and is at a stage of development at which it is still actively growing, it will react rapidly to changes in radiation, *i.e.* it is in a radiation-limited regime. Under the conditions of our study, stomata appear to have reacted only slowly or remained constantly open, because leaves were unstressed or reacting only slowly to cloud-induced changes. Moreover, the timescale of a light-induced stomatal response (maximum values twenty minutes, Van Keesteren, 2013b) is normally larger than the timescale of most fluctuations in radiation. Our suggested explanation is that the one- to two-minute delay time observed between radiation and turbulent fluxes is due to processes associated to an inertia of the leaf in addition to turbulent transport between the leaf and laser path due to e.g. the small but not negligible storage of heat,  $H_2O$  and  $CO_2$  in the canopy layer. However, we need further evidence to disentangle the separation in delays between  $CO_2$  and water vapor fluxes.

### 3.4 Sun induced fluorescence (SIF) measurements

#### 3.4.1 Local measurements of spatial and temporal dynamics of SIF

A key goal of CloudRoots was to study spatial and seasonal variabilities in evapotranspiration during plant growth. To this end, we included SIF observations. The top-of-canopy measurements of SIF were carried out in two ways: (i) diurnal courses from a single representative location were recorded from a stationary FLOX system, and (ii) mobile measurements covering several locations within a field were recorded from a FLOX system that was housed in a backpack. To ensure reproducible measurements the two fibre optics of the system were attached to a gimbal and were placed with a movable tripod 2 meters above ground.. Diurnal evolution curves were acquired on 7<sup>th</sup> May, 4<sup>th</sup> June, 4<sup>th</sup>, and 14<sup>th</sup> June (only morning hours due to cloudy conditions in afternoon); mobile measurements (with change of measurement locations during the day) on 6<sup>th</sup> June and 26<sup>th</sup> June. As SIF measurements should be performed under clear-sky conditions only, records affected by clouds were carefully removed. Fig. 13a shows the aerial map of  $F_{760}$  acquired on June 26<sup>th</sup>, suggesting homogeneous canopy properties across the winter wheat study field compared with contrasts between different fields. The same image identifies the FloxBBox measurement locations in the same colour code that shows the diurnal temporal variability of  $F_{760}$  during the entire CloudRoots campaign in Fig. 13b. The standard deviation of  $F_{760}$  is also shown.



Diurnal changes in photosynthetic activity are clearly visible in  $F_{760}$ . Measurements made at different locations generally follow the same diurnal pattern, especially within the period 7<sup>th</sup> May to 14<sup>th</sup> June, further confirming the hypothesis that spatial heterogeneity within the field was small. The seasonal changes are also traced by  $F_{760}$ : From 7<sup>th</sup> May until 14<sup>th</sup> June, the winter wheat canopy was photosynthetically active in a transition stage from booting (7<sup>th</sup> May) until grain filling (14<sup>th</sup> June), as is reflected by high SIF values. At the end of June, however, the canopy approached senescence and the reduction in photosynthesis was documented by greatly reduced fluorescence levels (see Fig. 13b). A similar pattern is found in the normalised difference vegetation index (NDVI): the green dense canopy has a NDVI value close to 1, and the decrease in NDVI is caused by the yellowish colour of the winter wheat canopy (see Fig. 14). The pattern closely follows that shown in Fig. 3c for maximum light-saturated photosynthesis, and is in line with the very low values of leaf-level stomatal conductance during IOP 3.

### 3.4.2 Regional measurements linking SIF to evapotranspiration

It is difficult to directly resolve spatial variations in evapotranspiration fluxes with the currently available in-situ equipment due to the necessity of installing a large number of measurement stations. To cover this gap, we link evapotranspiration (ET) with regional measurements of SIF, which were recorded on this scale by dedicated airborne sensors. Currently several activities are ongoing that test the potential of SIF to better predict plant water status and evapotranspiration (see Damm et al 2018 for a recent overview). For this study we used the 15 km x 15 km map acquired by the HyPlant sensor on 26<sup>th</sup> June 2019 and a land use classification of the region (Lussem, 2018). ET was estimated by using different  $K_c$  coefficients for different land use categories. Here,  $K_c$  is the ratio of ET over a particular crop relative to the ET of potential grass used as reference (Allen, et al., 1998; Bogena, et al., 2010)

For this analysis, a land-use classification with a small number of classes was introduced: "impervious" (see Table 4), "bare soil", "early crops (cereals)", "late crops (sugar beet, potato, corn, root crops)", "grassland" and "forest". Rapeseed fields were classified as "bare soil", since they were almost bare until end of June. Smaller roads were excluded from the analyses, as their area would be overestimated with pixel size of 15x15 m, and they are covered by a large variety of surfaces that range from asphalt or bare soil to grass. Residential areas were also excluded from the analyses as the proportion of non-evapotranspiration areas (roads, houses, parking lots) to vegetated areas with different  $K_c$  coefficients (lawn, grass, deciduous/coniferous trees, vegetables, etc.) is unknown. For the estimation of  $K_c$  evapotranspiration coefficients, the developmental stage at the CloudRoots site at the end of June, was defined, and the typical values of  $K_c$  for the crop and the developmental stage were subsequently taken from Allen et al. (1998). However, for the main regional crops, namely sugar beet, winter wheat, winter barley, and potatoes, local measurements of evapotranspiration by EC towers could be used. These data have been collected over several years and weekly averaged, finally computing  $K_c$  from measured and potential ET averaged over the last two weeks of June. In the cases of winter wheat and especially winter barley, the  $K_c$  coefficient changes rapidly at this time of the year, in extreme cases from 1.0 to 0.3 within two weeks, due to the onset of senescence.



Therefore, the coefficients for these two crops are tentative. The estimated  $K_c$  coefficients for different crops can be found in Table 4. To estimate the evapotranspiration over a specific area occupied by particular crop on a given day and time, the land-use map was transferred to the map of  $K_c$  coefficients according to Table 4 and then multiplied by the potential ET, using the ET<sub>grass</sub> as a reference value (ET<sub>grass</sub>), specific to that moment in time.

5 Fig. 15 shows the correlation between estimated evapotranspiration and fluorescence calculated for 26th June (Julian day 177). As the HyPlant overflight was carried out at noon in order to acquire the maximal SIF values and minimize the influence of changing sun angle, we also used the maximal value of ET<sub>grass</sub>, measured at midday on 26<sup>th</sup> June: ET0\_grass\_max = 8.077 mmol m<sup>-2</sup> s<sup>-1</sup>. Except for the category “impervious”, the inferred values were within the range of evapotranspiration as measured by other instruments, *i.e.* between 3 to 6 8.077 mmol m<sup>-2</sup> s<sup>-1</sup>. In consequence, and as a first  
10 approximation for the modelling of regional average fluxes (see Sec. 3.5), we reduced the number of land categories to only two: “bare soil/impervious” and “vegetated”.

For IOP 3, Fig. 16 shows the spatial variability of evapotranspiration inferred using the same method based on the  $K_c$  coefficients and the value of potential grass reference ET, averaged between 09:00 am and 14:00 pm. The area is a 1 km x 1 km square, characterized by a mean of 5.76 mmol m<sup>-2</sup> s<sup>-1</sup> and a standard deviation of 1.86 mmol m<sup>-2</sup> s<sup>-1</sup>. Fig. 16 shows that  
15 this method can provide useful information on the variability of ET at the sub-kilometre scale and it points out to the need to introduce this sub-grid ET variability information in modelling studies.

### 3.5 Boundary-layer integrated dynamics over heterogeneous landscapes

To integrate and improve the interpretation of our observations, we used CLASS to model the cloudless day 7<sup>th</sup> May 2018 (IOP 1). Our specific aims, related to the scales and processes under study, are: (i) at leaf level, to make use of the new  
20 constants in the mechanistic A-g<sub>s</sub> model obtained from the observations (Fig.5 and Table 3), (ii) at landscape scale, to represent the sensible heat flux in a heterogeneous landscape and (iii) to estimate the potential impact of advection (heat) on the diurnal evolution of surface and boundary-layer variables. Table A2 summarises all initial and boundary conditions, constrained by the observations, which are employed in the modelling of the surface and atmospheric variables. Fig. 17 compares the model results with the surface and upper-air observations. Focusing first on Fig. 17a, we found that the  
25 modelled  $H$  largely overestimates the observations taken at the CloudRoots. However, comparing our modelled  $H$  with the estimate of the regional flux shown in Fig. 1c, we found a satisfactory agreement in terms of magnitude and diurnal variability between this regional observed flux and CLASS model calculation. We suggest the following explanation: in a heterogeneous landscape such as the location of CloudRoots (Fig. 1a), each surface type contributes its own latent and sensible heat fluxes. It is the landscape aggregate of heat fluxes (named regional and shown with triangles in Fig. 17a and  
30 introduced in Fig. 1c), and more specifically the sensible heat flux, that governs the boundary-layer evolution in terms of height, potential temperature, specific humidity and atmospheric constituents. Only by using this higher  $H$  do we obtain satisfactory agreement with the observed boundary-layer height evolution, which reaches its maximum values at around 1500 m in the afternoon (Fig 8b). This further emphasises that the  $H$  measured with the EC instrument during CloudRoots is



only representative of the specific measurement site (leaf and canopy scales). The landscape average is an aggregate of values of  $H$  made up of the mosaic of surfaces as shown in Fig.1. As a consequence, it is this composite  $H$  rather than, a local value of  $H$ , that is the main driver of the boundary-layer development (boundary-layer scales). With regard to ET, it the model results are in good agreement with the local CloudRoots observations. This indicates the secondary and more local  
5 role played by ET in the dynamics of boundary layer development. For studies focusing on the regional values of ET, it will be necessary to calculated landscape-scale aggregate following the same procedures as  $H$ , while for studies at the leaf and canopy scales the local observations of ET are representative. Focusing now on Fig 17b, we found a satisfactory agreement between the modelled boundary-layer height and the three independent observations made with three different instruments. In this Fig. 17b, it is interesting to note that the ABL height inferred by the radio sounding measurement collected more than  
10 100 km distant from of the Cloud Roots site has values similar to those collected by the LIDAR located within a radius of 5 km from the CloudRoots site. We attribute these similar values to a boundary layer that is characterized by being spatial homogeneous and with a similar temporal evolution on the larger regional scale.

In CLASS, besides solving the diurnal variability of the boundary-layer dynamics and the state variables, offers the possibility of adding a large-scale contribution that represents the advection of heat and/or moisture (see Vilà-Guerau de  
15 Arellano et al., 2015). We have performed a sensitivity analysis to determine the role played by heat advection for the surface fluxes and the boundary-layer development. In the specific case that is modelled on 7<sup>th</sup> May 2018, we relate this advection of heat or moisture to the diurnal evolution of  $H$  contrast between the measurement site and its adjacent fields, i.e. horizontal transport of heat, moisture or momentum is driven by secondary circulations induced by the different thermal characteristics of the fields around the CloudRoots site (Fig. 1a). More specifically, we prescribe an advective heat  
20 contribution to represent the horizontal transport of heat due to the thermal variability of the surface conditions. This term follows an exponential function (Table A2) with maximum positive values of advection equal to  $0.9 \text{ K h}^{-1}$  at midday. This advective term is imposed only on the mixed-layer and not on the free troposphere. Fig. 17 shows how this advection of warm air to the CloudRoots site influences the boundary-layer height. Starting with SH, warm advection leads to higher temperatures that reduce the gradient between the temperature at the surface and the atmosphere, and thus reduce the  
25 sensible heat flux. We find an opposite effect on ET. The increase in temperature by advection of warm air leads to an increased atmospheric demand, and therefore enhances ET. With regard to the boundary-layer height, we might suppose that a drop in of SH would lead to a decrease of the boundary-layer growth. However, the modelled boundary-layer height displays the opposite behaviour. This is because the lower SH is partly offset by a decrease in the thermal inversion at the interface between the boundary layer and the free troposphere. Lower values of the difference in  $\theta_v$  between the free  
30 troposphere and the mixed-layer enable boundary-layer air parcels to be more easily transported into the free troposphere, resulting in faster growth of the boundary-layer. This is because of the virtual potential temperature between the environmental and the parcel is effectively reduced. The CLASS model results show that this process is more important than the decrease in SH at the surface, and it allows the boundary layer to grow deeper than in the numerical experiment in which the warm advection is omitted. These numerical sensitivity experiment analyses enable us to quantify how non-local



processes, in particular the effects of the regional average SH and of warm advection, influence the observations at the measurement site.

#### 4 Discussion

CloudRoots offers an integrated methodology that combines field experiments across spatial scales (from leaf to landscape) closely linked to the modelling of the diurnal variability of the soil-plant-atmosphere continuum. To frame the discussion and link all our observations and modelling efforts, we present in Fig. 18 all the different estimates of ET obtained during the three IOPs, averaged between 9 and 14 UTC in order to avoid the morning and afternoon transitions. Plotted alongside the ET estimates, we plotted the leaf-level measurement of  $g_{sw}$  to indicate the control of vegetation on canopy-level ET. The four instrumental techniques are: sap flow, the eddy-covariance (EC), scintillometer (averaged over 30 minutes and 1 minute), ET inferred by the profile lift measurements and ET infrared from the SIF observations. The ET modelled by CLASS is also included for IOP 1.

In comparing ET from the three IOPs, we find significant differences in magnitude from different techniques. In general, the highest values of ET are observed during IOP 1. The three IOPs were characterized by differences in the stages of growth, from very active vegetation to senescent, and influenced by a range of weather conditions: IOP 1 cloudless, IOP 2 scattered and thick clouds, and IOP 3 shallow cumuli. It is surprising that the decay in the vegetation activity as quantified by the measurements of leaf conductivity (Fig. 3 lower panels) is less evident in differentiating IOP 3 (senescent stage) from the more active vegetation at IOP 1 and 2. Furthermore we observed, moving from IOP 1 to IOP 3, a much stronger decline in  $g_{sw}$ , suggesting that stomatal closure compensated for increased atmospheric moisture demand.

Several conclusions can be drawn from this intercomparison of ET observations using different techniques. Firstly, we might expect that the EC/scintillometer measurements, both with larger footprint and the inclusion of the soil evaporation contribution, show a net total ET that is similar to or higher than that one obtained by the sap-flow measurements. Secondly, we observed a far more pronounced response in declining  $g_{sw}$  compared to all ET measurements. These results point to the need to measure more accurately the leaf energy balance to take the penetration of radiation in the canopy under clear and cloudy conditions into account. This would also require a revision of scaling procedure from the leaf to the canopy level. Secondly, it is known that the EC flux measurements normally underestimate the sensible and latent heat fluxes because the EC flux measurements filter out the low frequencies (Foken et al., 2008; Gao et al., 2017). This underestimation is difficult to determine, but as a first-guess and related to Fig. 18 the underestimation might range between 10 and 15%.

Although the contribution of soil evaporation is small compared to plant transpiration due to the high vegetation cover, we need to stress that EC and scintillometer observations are similar to or smaller than the ET observed or inferred from the other techniques (Fig. 18). This highlights the difficulty of estimating ET due to the need to include and quantify the contributions of the four fundamental processes: soil evaporation, up-scaled leaf transpiration, evaporation related to the sap flow and the two non-local processes, entrainment of dry air and horizontal advection of heat and moisture. Here, the



modelling of ET, taking into account for and integrating all these processes, enables us to discriminate among these processes and calculate the budget of ET as a function of these local and non-local contributions. In that respect, the CLASS model is a tool capable of efficiently combining observations and model results that integrate surface and boundary-layer dynamics. The averaged modelled ET is at the higher range of the ET observed estimations during IOP 1.

5 With respect to the differences between the 1-minute and 30-minute series measured by the scintillometer, their median is very similar in the three IOPs. However, differences become larger at smaller timescales due to the non-steadiness of evapotranspiration under the presence of clouds. Here, the one-minute flux calculated from the scintillometer can capture the rapid and large fluctuations by clouds (Fig. 11 and 12), and in particular the maximum values. In order to obtain more definitive conclusions how ET varies under cloud conditions, we need to analyse in more detail other situations characterized  
10 by different diurnal cloud cycles, and systematically relate ET to key cloud characteristics such as the cloud optimal depth to determine how cloud thickness influences ET, and the time scale of the cloud passage.

Regarding the quantification of the different processes contributing to ET, Fig. 9 illustrates the need to continue to test analytical techniques to identify the individual contributions of soil and plants to determine the diurnal ET budget. A possibly useful tracer would be the stable isotopic composition of water vapour and carbon dioxide (Lee, et al., 2009; Griffis,  
15 2013) and combined with isotope signals in modelling the surface and boundary-layer dynamics with the carbon and water exchanges. To further discriminate between soil and plant sources and sinks under unsteady conditions due to radiation and dynamic perturbations by cloud shading, these high-frequency stable isotope measurements should go beyond the typical average time of eddy-covariance (30 minutes). As van Kesteren et al. (2013) showed, and is further corroborated in this work, the scintillometer technique combined with high-frequency observations of H<sub>2</sub>O and CO<sub>2</sub> enable us to quantify the  
20 responses time of ET and CO<sub>2</sub> assimilation to these intermittent radiation fluctuations or cloud flecks (Kaiser et al., 2018).

Finally, the integration of all processes in the CLASS model shows the challenges in interpreting the measurements taken at the sub-kilometre scales and adequately representing the surface turbulent fluxes. Although the measurements indicate that the day selected for the modelling displayed a very homogeneous boundary layer depth over an area with a radius of 100 km<sup>2</sup>, the sensible heat flux measured at the CloudRoots facility was not representative of it. Therefore, recommend to  
25 extending the number of stations by means of a multi-tower approach that would also include also detailed observations of the soil and plant conditions. In addition to obtaining a more representative field sensible heat flux which is better related to the development of the boundary layer, a denser network of spatial observation stations is also necessary to more accurate estimate the role of hectometre-scale heterogeneity-induced circulations and their relationships with the local advection of heat and moisture (Mauder, et al., 2010).

## 30 5. Conclusions



Our main findings, organised from the smaller to the larger scales observed and modelled, are summarized as follows:

- At *leaf scale*, we find that stomatal conductance and gross primary production decrease in line with the increasing senescence of the plant. The tiller-level measurements of the sap flow are virtually constant throughout the growing period. Underlying causes need to be further investigated under controlled conditions. The successful modelling of the leaf stomatal conductance and the photosynthesis assimilations required the relevant constants used in the mechanistic model ( $A-g_s$ ) in the field to be measured. For future field experiments, we recommend of including leaf-level measurements in meteorological campaigns to improve calculations related to the water-carbon leaf and canopy exchanges.
- At *canopy scale*, the high frequency vertical profiles – measured in and above the canopy - of wind speed, potential temperature, specific humidity and carbon dioxide prove to be very valuable in obtaining profiles of gross primary production in the canopy and as a function of height. By inverting these observed profiles, we obtain an estimate on the contributions of soils and plants to the net evapotranspiration and ecosystem exchange. The validation against individual measurements of these components gives better results for the net ecosystem exchange than those the net evapotranspiration. We argue that for evapotranspiration the dependence on temperature and water vapor deficit plays a more important role than for  $\text{CO}_2$  assimilation, the latter being mainly controlled by the partitioning between direct and diffuse radiation.
- Under *cloud conditions*, we show that the perturbation by clouds of direct and diffuse radiation create large fluctuations on the  $\text{CO}_2$  assimilation and evapotranspiration. This impacts of opposite signs for evapotranspiration and  $\text{CO}_2$  exchange. A cloudy boundary layer reduces evapotranspiration, whereas it enhances plant assimilation of  $\text{CO}_2$ . The one-minute turbulent fluxes acquired by the scintillometer demonstrate the relevance of flux measurements observed at higher frequencies to improving quantification of the impact of clouds on the photosynthetically active radiation. With these fast-turbulent fluxes, we quantify delays of the turbulent fluxes with respect to PAR. These delays are on the order of minutes. Comparing these 1-minute flux estimate with the standard thirty-minute average measured with the eddy-covariance technique, we find a lower median and a large increase in the variability of the net evapotranspiration. This information can be useful in determining the impact of rapid fluctuations driven by the impact of clouds on evapotranspiration and its impact on the closure of the surface energy balance.
- At *boundary-layer integrated scale*, the modelled sensible heat flux correlates better with the area-weighted average flux than the local flux estimates. The area-weighted flux integrates in a simple manner a composite of bare soil and vegetated surfaces at regional scale (kilometres). This aggregate regional flux is representative of an area that is larger than the CloudRoots site (100 m x 100 m). The impact of surface heterogeneity was further studied using ET estimates inferred from the fluorescence data. The analysis



5

indicates a rather homogeneous values for grass, crops and forest. Therefore, a model setup that represents the boundary layer evolution well only needed to be informed by the area-weighted average of two main surface types, bare soil and vegetated areas. The comprehensive observational data set enables us to validate the carbon and water exchange at leaf and canopy level as well as to quantify how horizontal advection of heat within the mixed-layer influences the surface fluxes and the growth of the atmospheric-boundary layer. We show that the horizontal advection of heat leads to deeper boundary-layer depths. This numerical experiment thus paves the way to more complete modelling studies on how surface and the overlaying atmosphere interact on sub-diurnal scales.

## 10 6. Author Contributions

JVG designed the CloudRoots study and approach. OH and AG designed and coordinated the CloudRoots field experiment. The individual measurements were gathered by: OH (scintillometer), HB (stomatal aperture/photosynthesis), AK and AG (elevator profiles), ML (sap flow), MM and DA, TR and GA (stable isotopes). HB integrated the observations to be connected with the modelling efforts. GG, GM, HB and JVG performed the numerical experiments with CLASS. PN and JVG wrote the paper with key contributions from all the authors: OH, HB, KD, DE, GG, AK, ML, MM, GM, AM, UR, TR, GA and AF.

## 7. Data availability

All CloudRoots observations are archived at <https://www.tr32db.uni-koeln.de> and the search term “cloudroots”). The data can be obtained upon request at Only CRC/TR32 participants are allowed to apply for an account. Please contact the TR32DB admin for further information. CLASS model (Python and Fortran versions) is freely available at <http://classmodel.github.io/>.

## 8. Acknowledgements

This study was financed by the Deutsche Forschungsgemeinschaft (DFG) Collaborative Research Centre 32 (TR32) “Patterns in Soil-Vegetation-Atmosphere System”. The contribution of AG and deployment of the profile elevator, microlysimeter and part of the isotope measurements were financed by the German Federal Ministry of Education and Research (BMBF) within the framework of the project “IDAS-GHG“ (Grant: FKZ 01LN1313A). Airborne acquisition and data analysis with the HyPlant sensor were financed by the European Space Agency (ESA) in the frame of the FLEXSense campaign (ESA Contract No. ESA RFP/3-15477/18/NL/NA). The contribution of PN to the analysis were financed by the European Space Agency (ESA) within the project PhotoProxy (Grant. ESA RFP/3-15506/18/NL/NF). The ancillary hardware and its maintenance were supported by TERENO (<https://www.tereno.net>). The authors wish to thank Bernhard Pospichal and Tobias Marke for contributing measurements on boundary layer properties. These data were provided by the Jülich Observatory for Cloud Evolution (JOYCE-CF), a core facility funded by DFG via grant DFG LO 901/7-1. Hubert



Hüging and Huu Thuy Nguyen from the INRES Crop Science Group of Bonn University for operating the sap-flow equipment.

## References

- Allen, R., Pereira, L., Raes, D., & Smith, M. (1998). Crop evapotranspiration: Guidelines for computing crop water requirements. *Food and Agriculture Organization of the U.N. Irrigation and Drainage Paper*(56), 300 pp.
- 5 Baker, J. M. & van Bavel, C. H. (1987). Measurement of mass flow of water in the stems of herbaceous plants. *Plant, Cell and Environment*, 9(10), 777-782.
- Bogena, H., Herbst, M., Huisman, J., Rosenbaum, U., Weuthen, A., & Vereecken, H. (2010). Potential of Wireless Sensor Networks for Measuring Soil Water Content Variability. *Vadose Zone Journal*, 9(4), 1002-1013.
- 10 Boussetta, S., Balsamo, G., Beljaars, A., Panareda, A.-A., Calvet, J.-C., Jacobs, C., . . . Van der Werft, G. (2013). Natural land carbon dioxide exchanges in the ECMWF Integrated Forecasting System: Implementation and offline validation. *Journal of Geophysical Research: Atmospheres*, 118(12), 5923-5946.
- Campbell, P., Huemmrich, K., Middleton, E. *et al.* Diurnal and Seasonal Variations in Chlorophyll Fluorescence Associated with Photosynthesis at Leaf and Canopy Scales. (2019) *Remote Sensing*, 11(5), 488-515.
- 15 Cava, D., Katul, G., Scrimieri, A., Poggi, D., Cescatti, A. & Giostra, U. (2006). Buoyancy and the sensible heat flux budget within dense canopies. *Boundary-Layer Meteorology*, 118(1), 214-240.
- Damm A., Paul-Limoges E., Haghghi E., Simmer C., Morsdorf F., Schneider F.D., van der Tol C., Migliavacca M. & Rascher U. (2018) Remote sensing of plant-water relations: An overview and future perspectives. *Journal of Plant Physiology*, 227, 3-19, doi: 10.1016/j.jplph.2018.04.012.
- 20 Dengel, S., & Grace, J. (2010). Carbon dioxide exchange and canopy conductance of two coniferous forests under various sky conditions. *Ecosystem Ecology*, 3, 797-808.
- Dynamax. (2007). *Dynagage Sap Flow Sensor User Manual*. Accessed 29-07-2019 at [http://dynamax.com/images/uploads/papers/Dynagage\\_Manual.pdf](http://dynamax.com/images/uploads/papers/Dynagage_Manual.pdf)
- Dynamax. (2017). *Flow32-1K Sap Flow Monitoring System Installation & Operation Manual*. Accessed 29-07-2019 at
- 25 [http://www.dynamax.com/images/uploads/papers/Flow32-1K\\_Manual.pdf](http://www.dynamax.com/images/uploads/papers/Flow32-1K_Manual.pdf)
- Farquhar, G. D. & Roderick, M. L. (2003). Pinatubo, diffuse light, and the carbon cycle. *Science*, 5615, 1997-1998.
- Franz, D., Acosta, M., Altimir, N., Arriga, N., Arrouays, D., Aubinet, M., . . . Berveiller, D. (2018). Towards long-term standardised carbon and greenhouse gas observations for monitoring Europe's terrestrial ecosystems: a review. *International Agrophysics*, 32(4),439-455.
- 30 Foken, T., (2008). The energy balance closure problem: an overview. *Ecological Applications* 18, 1351-67.
- Gao, G., Liu, H., Katul, G.G. & Foken, T., (2017) Non-closure of the surface energy balance explained by phase differences between vertical velocity and scalars of a large atmospheric eddies. *Environmental Research Letters* 12, 034025.



- Goudriaan, J. (1986). A simple and fast numerical method for the computation of daily totals of crop photosynthesis. *Agriculture and Forest Meteorology*, 38, 249-254.
- Griffis, T. J. (2013). Tracing the flow of carbon dioxide and water vapor between the biosphere and atmosphere: A review of optical isotope techniques and their application. *Agricultural and Forest Meteorology*, 174-175, 85-109.
- 5 Gryning, S. E., de Bruin, H & Batchvarova, E., (2001). Energy balance of a sparse coniferous high-latitude forest. *Boundary-Layer Meteorology*, 99(3), 465-488.
- IUSS Working Group WRB. (2006). *World Reference Base for Soil Resources 2006*. FAO Rome: World Soil Resources Reports 103.
- Jacobs, C. M., & de Bruin, H. A. (1997). Predicting regional transpiration at elevated atmospheric CO<sub>2</sub>: influence of the PBL–vegetation interaction. *Journal of Applied Meteorology* 36, 1663-1675.
- 10 Kanniah, K. D., Beringer, J., North, P., & Hutley, L. (2012). Control of atmospheric particles on diffuse radiation and terrestrial plant productivity: A review. *Progress in Physical Geography*, 2, 209-237.
- Katul, G. G., Oren, R., Manzoni, S., Higgins, C., & Parlange, M. B. (2012). Evapotranspiration: A process driving mass transport and energy exchange in the soil-plant-atmosphere-climate system. *Reviews of Geophysics*, RG3002.
- 15 Knohl, A. & Baldocchi, D. D. (2008). Effects of diffuse radiation on canopy gas exchange processes in a forest ecosystem. *Journal of Geophysical Research*, G02023, 1-17.
- Langensiepen, M., Kupisch, M., Graf, A., Schmidt, M., & Ewert, F. (2014). Improving the stem heat balance method for determining sap-flow in wheat. *Agriculture, Forest and Meteorology* 186, 34-42.
- Lee, A. P., Upchurch, G. Jr., Murchie E. H. & Lomax, B. H. (2015) Leaf energy balance modelling as a tool to infer habitat preference in the early angiosperms. *Proceedings of the Royal Society B* 282, 20143052.
- 20 Lee, X., Griffis, T. J., Baker, J. M., Billmark, K. A., Kim, K., & Welp, L. R. (2009). Canopy-scale kinetic fractionation of atmospheric carbon dioxide and water vapor isotopes. *Global Biogeochemical Cycles*, 23, GB1002.
- Löhnert, U., Schween, J., Acquistapace, C., Ebell, K., Maahn, M., Barrera-Verdejo, M., . . . Crewell, S. (2015). JOYCE: Jülich Observatory for Cloud Evolution. *Bulletin of the American Meteorological Society* 96, 1157–1174.
- 25 Lussem, U. (2018). Land use classification of 2018 for the CRC/TR32 measurement region Selhausen/Merken/Merzenhausen, preliminary results. CRC/TR32 Database (TR32DB). DOI: [10.5880/TR32DB.32](https://doi.org/10.5880/TR32DB.32)
- Mauder, M., & Foken, T. (2011). Documentation and instruction manual of the eddy-covariance software package TK3, Internal Report 43, Department of Micrometeorology, University of Bayreuth, Bayreuth, Germany, pp 60. <https://epub.uni-bayreuth.de/342/1/ARBERG046.pdf>.
- 30 Mauder, M., Cuntz, M., Graf, A., Rebmann, C., Schmidt, H., & Steinbrecher, R. (2013). A strategy for quality and uncertainty assessment of eddy-covariance measurements. *Agriculture Forest Meteorology* 169, 122-135.
- Mauder, M., Desjardins, R. L., Pattey, E., & Worth, D. (2010). An attempt to close the daytime surface energy balance using spatially-averaged flux measurements. *Boundary-Layer Meteorology*, 136, 175–191.



- Moene, A. F. & Van Dam, J. C. (2014). *Transport in the atmosphere-vegetation-soil continuum*. Cambridge: Cambridge University Press, pp. 436.
- Monson, R. & Baldocchi, D. (2014). *Terrestrial Biosphere-Atmosphere Fluxes*. Cambridge: Cambridge University Press, pp. 487.
- 5 Nelder, J. A. & Mead, R. (1965). A simplex method for function minimization. *The Computer Journal*, 4, 308-313.
- Ney, P. & Graf, A. (2018). High-resolution vertical profile measurements for carbon dioxide and water vapour concentrations within and above crop canopies. *Boundary-Layer Meteorology*, 166, 449-473.
- Ney, P., Graf, A., Schmidt, M., & Vereecken, H. (2019). The carbon budget of a 3-year crop rotation: using three different nonlinear regression CO<sub>2</sub> flux partitioning approaches. *In preparation*.
- 10 Olesen, J., Hansen, P., Berntsen, J., & Christensen, S. (2004). Simulation of above-ground suppression of competing species and competition tolerance in winter wheat varieties. *Field Crops Research*, 89, 263-280.
- Pedruzo-Bagazgoitia, X., Ouwersloot, H. G., Sikma, M., van Heerwaarden, C. C., Jacobs, C. M., & Vilà-Guerau de Arellano, J. (2017). Direct and diffuse radiation in the shallow cumulus-vegetation system: enhanced and decreased evapotranspiration regimes. *Journal of Hydrometeorology*, 6, 1731-1748.
- 15 Quade, M., Klosterhalfen, A., Graf, A., Brüggemann, N., Hermes, N., Vereecken, H., & Rothfuss, Y. (2019). In-situ monitoring of soil water isotopic composition for partitioning of evapotranspiration during one growing season of sugar beet (*Beta vulgaris*). *Agriculture Forest and Meteorology* 165, 114-126.
- Rascher, U., Alonso, L., Burkart, A., Cilia, C., Cogliati, S., Colombo, R., . . . Pani. (2015). Sun-induced fluorescence - a new probe of photosynthesis: First maps from the imaging spectrometer HyPlant. *Global Change Biology*, 12, 4673-4684.
- 20 Rebmann, C., Aubinet, M. S., Arriga, N., Aurela, M., Burba, G., Clement, R., . . . Franz, D. (2018). ICOS eddy covariance flux-station site setup: a review. *International Agrophysics*, 32, 471-494.
- Reichstein, M., Falge, E., Baldocchi, D., Papale, D., Aubinet, M., Berbigier, P., . . . Yakir, D. (2005). On the separation of net ecosystem exchange into assimilation and ecosystem respiration. Review and improved algorithm. *Global Change Biology* 11, 1424-1439.
- 25 Roderick, M. L., Farquhar, G. D., Berry, S. L., & Noble, I. R. (2001). On the direct effect of clouds and atmospheric particles on the productivity and structure of vegetation. *Oecologia*, 1, 21-30.
- Ronda, R. J., De Bruin, H. A., & Holtslag, A. A. (2001). Representation of the canopy conductance in modeling the surface energy budget for low vegetation. *Journal of Applied Meteorology*, 40, 1431-1444.
- 30 Sakuratani, T. (1981). A heat balance method for measuring water flux in the stem of intact plants. *Journal of Agricultural Meteorology*, 1, 9-17.
- Santos, E. A., Wagner-Riddle, C., Warland, J., & Brown, S. (2011). Applying a Lagrangian dispersion analysis to infer carbon dioxide and latent heat fluxes in a corn canopy. *Agriculture Forest Meteorology*, 151, 620-632.



- Schmidt, M., Reichenau, T. G., Fiener, P., & Schneider, K. (2012). The carbon budget of a winter wheat field: An eddy covariance analysis of seasonal and inter-annual variability. *Agriculture Forest Meteorology*, 165, 114-126.
- Siegmann B., Alonso L., Celesti M., Cogliati S., Colombo R., Damm A., Douglas S., Guanter L., Hanuš J., Kataja K., Kraska T., Matveeva M., Moreno J., Muller O., Píkl M., Pinto F., Quirós Vargas J., Rademske P., Rodriguez-Moreno F., Sabater N., Schickling A., Schüttemeyer D., Zemek F. & Rascher U. (2019) The high-performance airborne imaging spectrometer HyPlant – From raw images to top-of-canopy reflectance and fluorescence products: Introduction of an automatized processing chain. *Remote Sensing* 11, doi: 10.3390/rs11232760.
- Sikma, M., Ouwersloot, H., Pedruzo-Bagazgoitia, X., Van Heerwaarden, C., & Vilà-Guerau de Arellano, J. (2018). Interactions between vegetation, atmospheric turbulence and clouds under a wide range of background wind conditions. *Agricultural and Forest Meteorology* 255, 31-43.
- Sikma, M. Ikawa, H., Heusinkveld, B.G., Yoshimoto, Y., Hasegawa, T., Groot Haar, L.T., Anten., N. P. R., Nakamura, H., Vilà-Guerau de Arellano, J., Sakai, H., Tokida, T., Usui, Y., Evers, J.B (2020) Quantifying the feedback between rice architecture, physiology and microclimate under current and future CO<sub>2</sub> conditions. *Journal Geophysical Research-Biogeosciences* 125, e2019JG005452.
- 15 Van Heerwaarden, C. C., & Teuling, A. J. (2014). Disentangling the response of forest and grassland energy exchange to heatwaves under idealized land-atmosphere coupling. *Biogeosciences*, 11, 6159-6171.
- Van Heerwaarden, C. C., Vilà-Guerau de Arellano, J., Gounou, A., Guichard, F., & Couvreur, F. (2010). Understanding the daily cycle of evapotranspiration: A method to quantify the influence of forcings and feedbacks. *Journal of Hydrometeorology*, 11, 1405-1422.
- 20 Van Kesteren, B., Hartogensis, O. k., Van Dinther, D., Moene, A., De Bruin, H. A., & Holtslag, A. A. (2013). Measuring H<sub>2</sub>O and CO<sub>2</sub> fluxes at field scales with scintillometry: Part II–Validation and application of 1-min flux estimates. *Agricultural and Forest Meteorology*, 178, 88-105.
- Vico, G., Manzoni, S., Palmroth, S., & Katul, G. (2011). Effects of stomatal delays on the economics of leaf gas exchange under intermittent light regimes. *New Phytologist*, 192, 640-652.
- 25 Vilà-Guerau de Arellano J., Ouwersloot H. G., Baldocchi D. & Jacobs C. M. J. (2014). *Shallow cumulus rooted in photosynthesis*. *Geophysical Research Letters* 41, 1796-1802.
- Vilà-Guerau de Arellano, J., Van Heerwaarden, C. C., Van Stratum, B. J., & Van den Dries, K. (2015). *Atmospheric boundary layer: Integrating air chemistry and land interactions*. Cambridge, Cambridge University Press, pp. 279.
- Vilà-Guerau de Arellano, J., Koren, G., Ouwersloot, H. G., van der Velde, I., Röckmann, T., & Miller, J. B. (2019). Sub-diurnal variability of the carbon dioxide and water vapor isotopologues at the field observational scale. *Agricultural and Forest Meteorology*, 275, 114-135.
- 30 Warland, J. S. & Thurtell, G. W. (2000). A Lagrangian solution to the relationship between a distributed source and concentration profile. *Boundary-Layer Meteorology*, 96, 453-471.

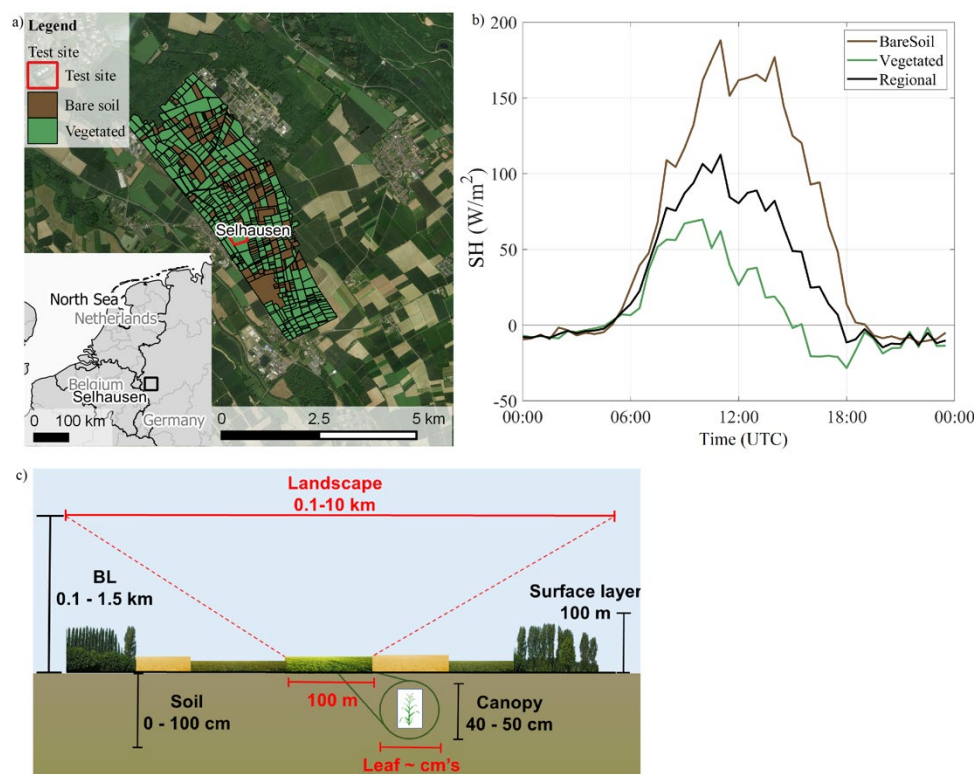


Wohlfahrt, G., Gerdel, K., Migliavacca, M. *et al.* Sun-induced fluorescence and gross primary productivity during a heat wave (2018). *Scientific Reports* 8, 14169, doi:10.1038/s41598-018-32602-z.

Wutzler, T., Lucas-Moffat, A., Migliavacca, M., Knauer, J., Sickel, K., Sigut, Menzer, O. & Reichstein, M (2018). Basic and extensible post-processing of eddy covariance flux data with REdyProc. *Biogeosciences*, 15, doi: [10.5194/bg-15-5015-2018](https://doi.org/10.5194/bg-15-5015-2018)

5

## Figures



10 **Figure 1:** Aerial view (Bing Maps, © 2019 Microsoft Corporation © 2019 DigitalGlobe © CNES (2019) Distribution Airbus DS) of the observation area. The ICOS Selhausen test site is located in the middle of the 10 x 10 km map section. The surrounding agricultural area was classified into the categories bare soil (including “late crops” after Table 3) and vegetated (“early crops”, forest and grassland after Table 3) during the IOP 1. b) Corresponding sensible heat flux ( $SH$ ) during IOP 1, whereby  $SH$  of bare soil and vegetated area were measured and the regional average was estimated as weighted average  
15 (60% and 40% for vegetated and bare soil, respectively). c) Schematic sketch of horizontal (red) and vertical (black) length scales influencing the measurements. The larger indicated horizontal and vertical scales indicate the spatial scales of boundary layer dynamics. Horizontally, the 100 m scale is the size of the field hosting the ICOS test site.

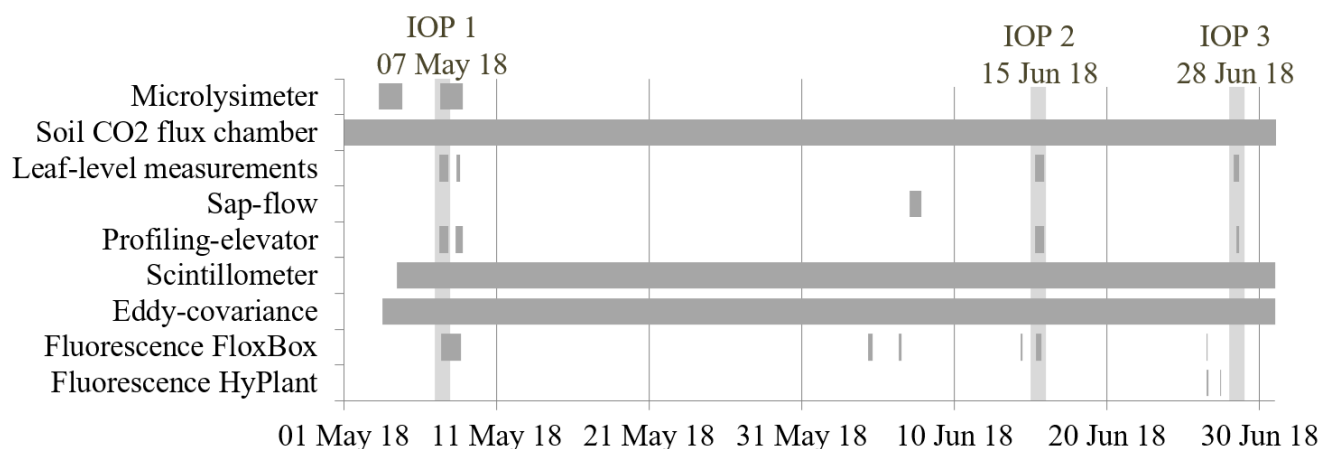


**Figure 2:** Campaign-specific measurement setup and temporal developments from May to June 2018, including three intensive operation periods (IOP).

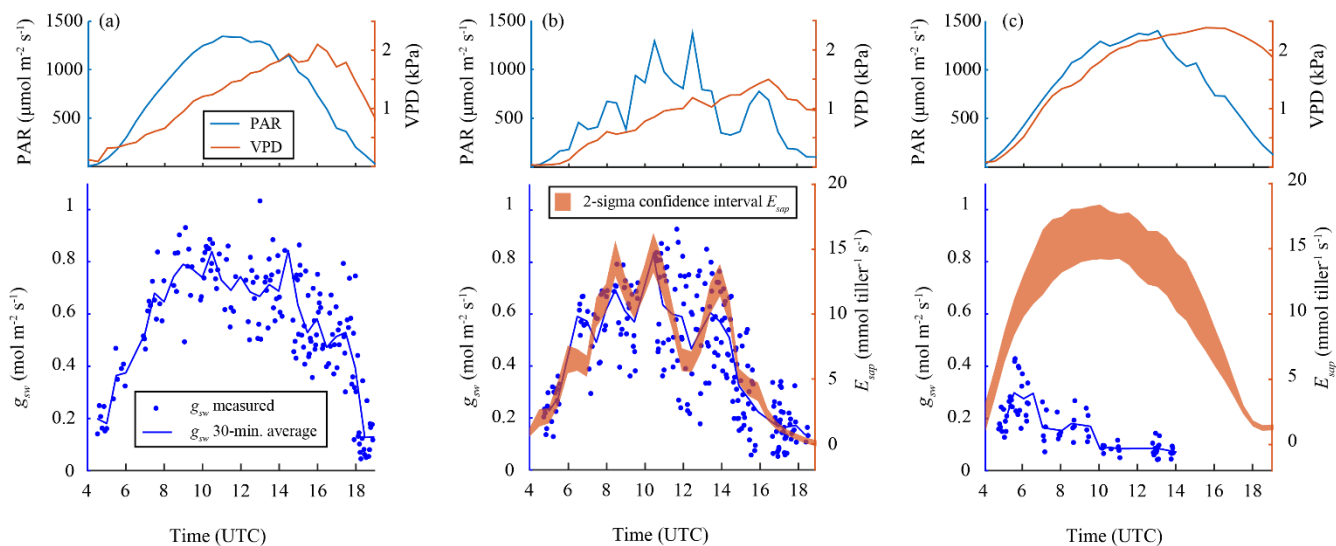


**Figure 3:** Upper panels: diurnal changes in photosynthetically active radiation (PAR) and vapour pressure deficit (VPD) measured for IOP 1 (a), IOP 2 (b) and IOP 3 (c). Lower panels: Leaf-level measurements of stomatal conductance of water vapour ( $g_{sw}$ ), in b) and c) compared to tiller-level measurements of sap flow ( $E_{sap}$ ). Leaf-level measurements of  $g_{sw}$  (blue markers) were averaged over 30-minute intervals (blue line). Sap flow measurements represent the one-standard-deviation confidence interval (shaded region) of measurements on 24 tillers averaged over 30-minute time scales.

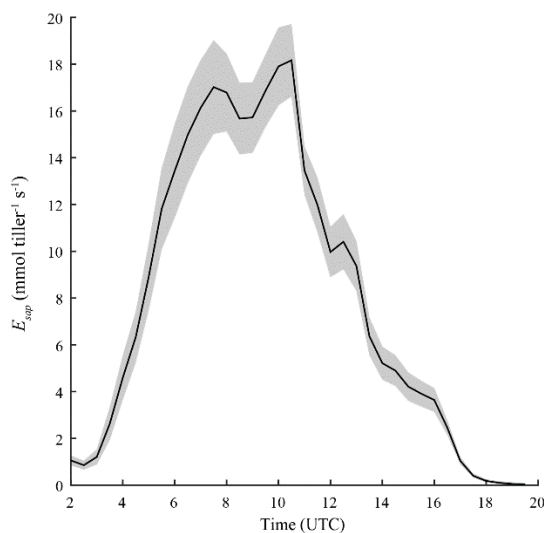


**Figure 3:** Sap-flow measured using the heat-balance method for 7 June 2018 (non-IOP day).

5

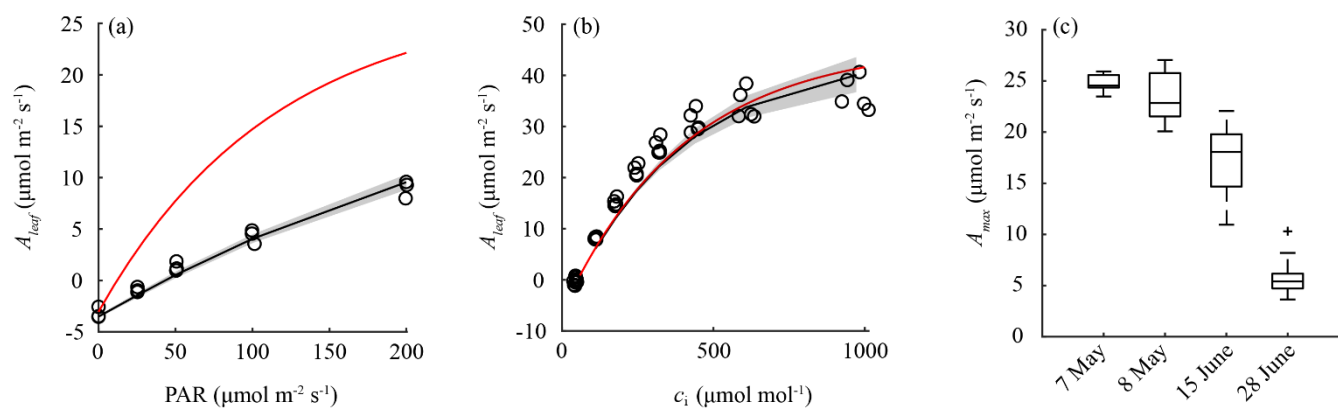


**Figure 5:** Measurements of leaf-level photosynthesis ( $A_{leaf}$ ) as function of photosynthetically active radiation (PAR) (a) and leaf-interior  $\text{CO}_2$  concentrations ( $c_i$ ) (b). These results were used to parameterize the A- $g_s$  model, as indicated by the black line and shaded one-standard-deviation confidence interval. The red line indicates the model response using the default parameter values (Table 3). (c) Observed seasonal decline in maximum light-saturated photosynthesis ( $A_{max}$ ).

10

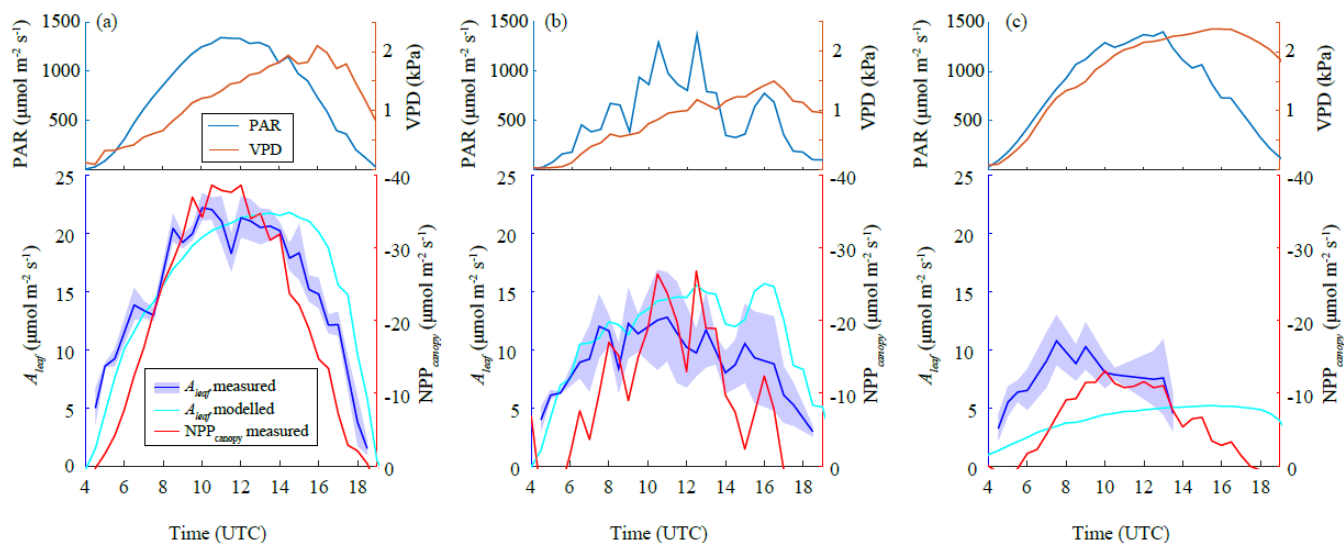


**Figure 6:** Measured leaf-level photosynthesis ( $A_{leaf}$ ) compared to modelled  $A_{leaf}$  using the A- $g_s$  model and canopy-level net primary productivity ( $NPP_{canopy}$ ) for IOP 1 (a), IOP 2 (b) and IOP 3 (c). Measurements of  $A_{leaf}$  were plotted as 30-minute averages (blue line) and their one-standard-deviation confidence interval (shaded region). Upper panels show diurnal changes in photosynthetically active radiation (PAR) and vapour pressure deficit (VPD) measured for each IOP.

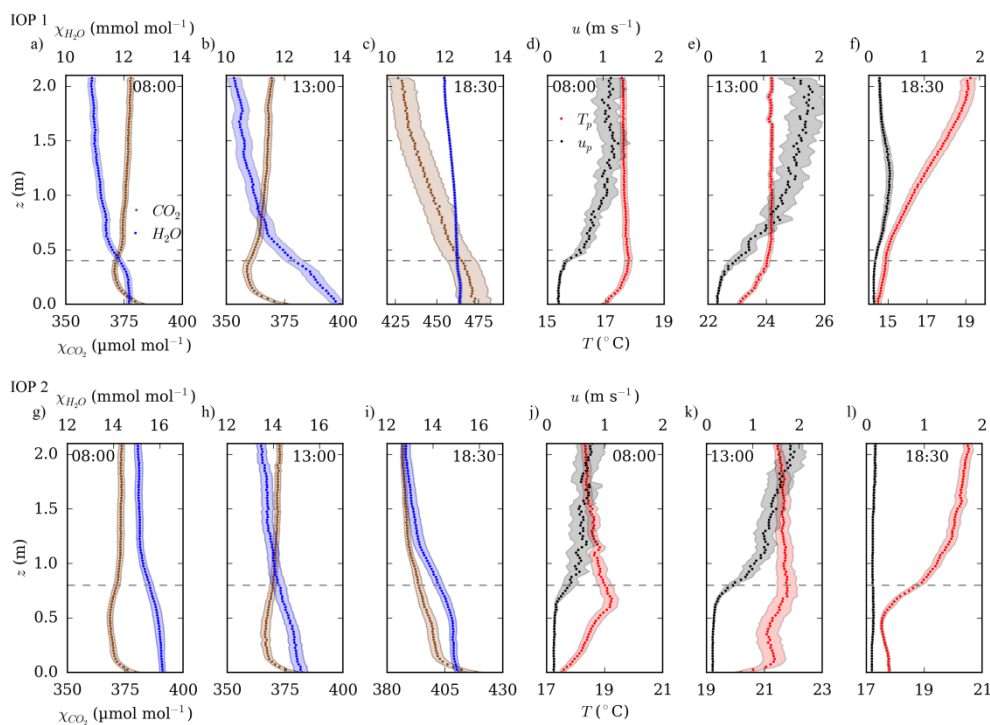


**Figure 7:** Selected (08:00, 13:00 and 18:30 UTC) 30-minutes mean profiles of  $\chi_{CO_2}$  and  $\chi_{H_2O}$ , wind speed  $u_p$  and temperature  $T_p$  measured at high vertical resolution during IOP 1 (upper panel) and IOP 2 (lower panel). Shaded areas indicate the 95 % confidence interval resulting from the standard deviation between individual profiles sampled within a 30-minute averaging interval.

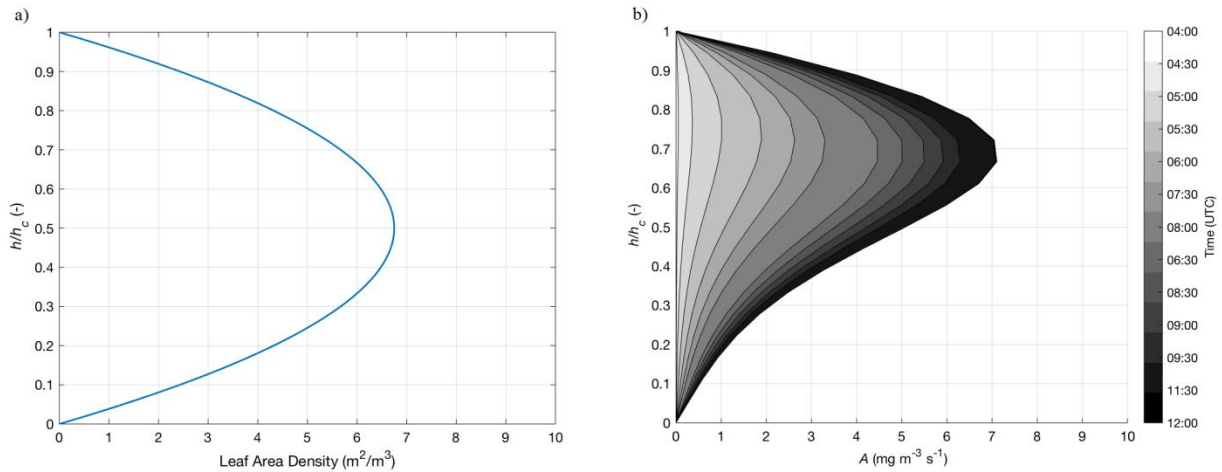


**Figure 8:** (a) Leaf area density ( $m_{\text{leaf}}^2 m^{-3}$ ) on 7 May 2018 as a function of height  $h$  (m) normalized to the canopy maximum  $h_c$  (m). The profile is typical for winter wheat as defined by (Olesen et al. 2004). (b) Time evolution of CO<sub>2</sub> gross primary production  $A$  ( $\text{mg m}^{-3} \text{s}^{-1}$ ) on 7<sup>th</sup> May 2018 as function of height  $h$  (m) normalized to the canopy maximum  $h_c$  (m).

5

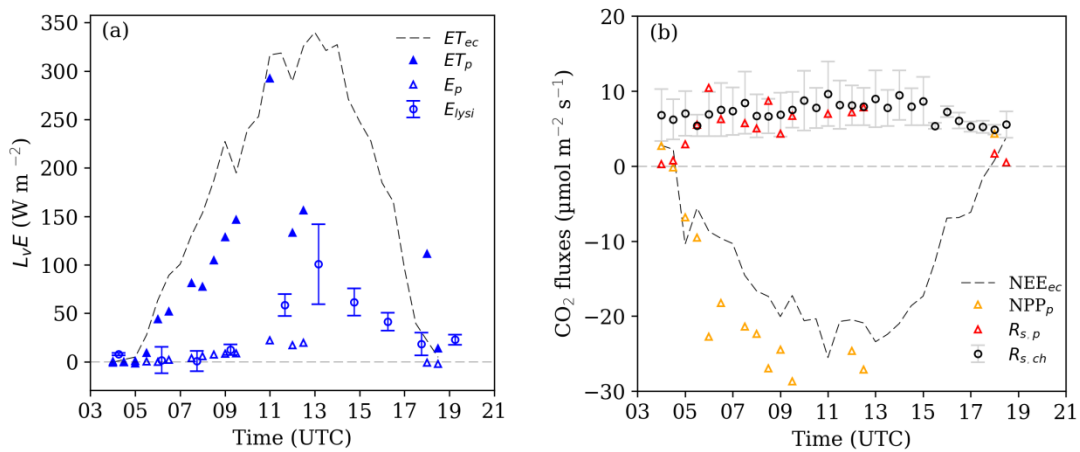


**Figure 9:** Source partitioning results for (a) H<sub>2</sub>O and (b) CO<sub>2</sub> fluxes for IOP 1. Grey dashed lines show the measured latent heat flux ( $ET_{ec}$ ) and net ecosystem exchange (NEE) in half-hourly time steps. Values with subscript index  $p$  indicate estimate based on inversed profile concentration measurements (Sec. 3.4). Error bars for evaporation calculated from microlysimeters ( $E_{lysi}$ ) and soil respiration measurements ( $R_{s,ch}$ ) indicated to one standard deviation. ( $ET_{ec}$ : evapotranspiration measured as latent heat flux  $L_vE$  by the eddy covariance system;  $E$ : evaporation; NPP: aboveground net primary production;  $R_s$ : soil respiration).

10

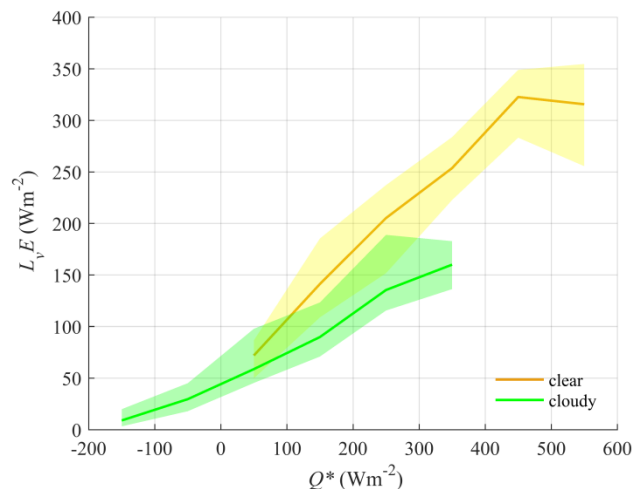


**Figure 10:** Latent heat ( $L_v E$ ) versus net radiation ( $Q^*$ ) for clear (yellow) and cloudy (green) skies during a two week-period starting on 7 May 2018 at 03:30 UTC (sunrise) and ending on the 20 May 2018 at 19:40 UTC (sunset). The solid line represents the median of the data. The lower and upper boundaries of the shaded area are the 25<sup>th</sup> and 75<sup>th</sup> percentiles of the data respectively.

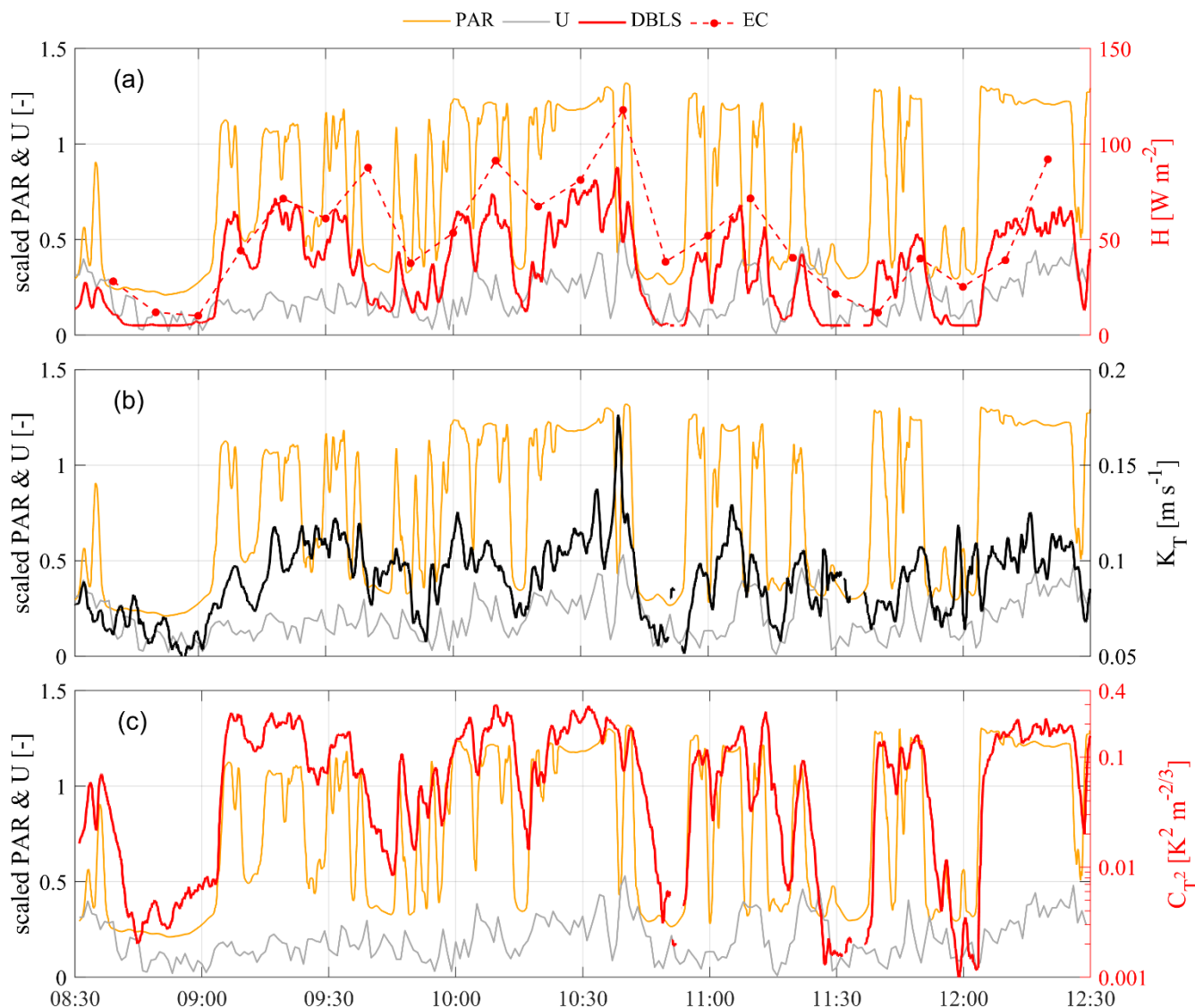


**Figure 11:** IOP 2 (15 June 2018) time-series of: (a) sensible heat fluxes ( $H$ ) at 1min intervals with a displaced beam laser scintillometer (DBLS) and at 10-minute intervals with an eddy-covariance system (EC), combined with scaled time-series of photosynthetically active radiation (PAR, scaled by  $1500 \mu\text{mol m}^{-2} \text{s}^{-1}$ ) and windspeed ( $U$ , scaled by  $6 \text{ m s}^{-1}$ ); (b) turbulent exchange coefficient  $K_T$  and (c) structure parameter of temperature,  $C_T^2$  that together make up  $H$  in the DBLS method following Eq. (2).

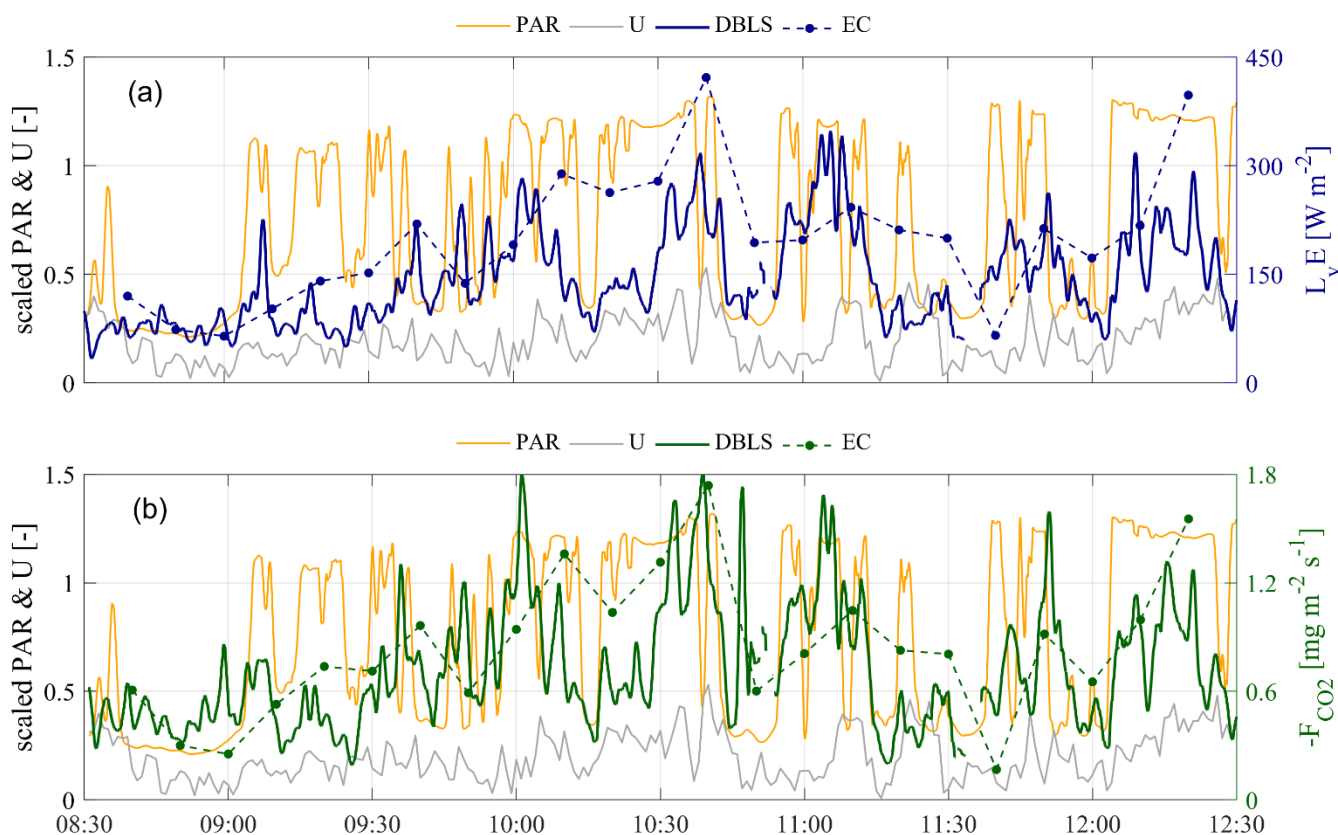


**Figure 12:** IOP 2 (15 June 2018) time-series of: (a) latent heat fluxes ( $L_vE$ ) at 1min intervals with a displaced beam laser scintillometer (DBLS) and at 10-minute intervals with an eddy-covariance system (EC) combined with scaled time-series of photosynthetically active radiation (PAR, scaled by  $1500 \mu\text{mol m}^{-2} \text{s}^{-1}$ ) and windspeed (U, scaled by  $6 \text{ ms}^{-1}$ ); (b) same as (a) but for the  $\text{CO}_2$  flux ( $F_{\text{CO}_2}$ ).

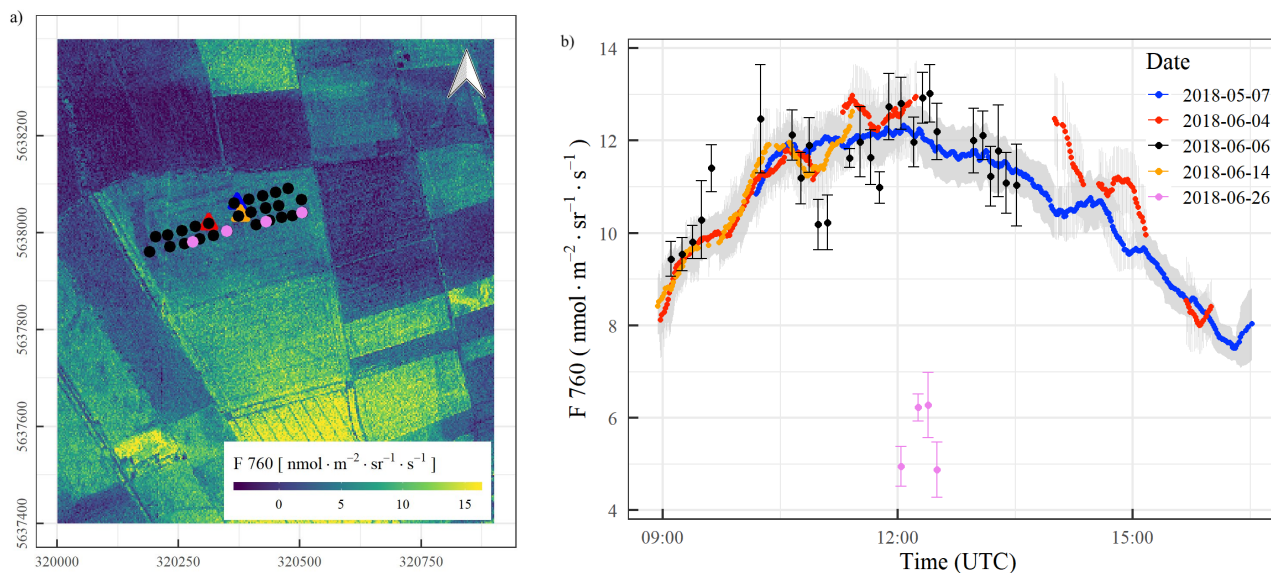
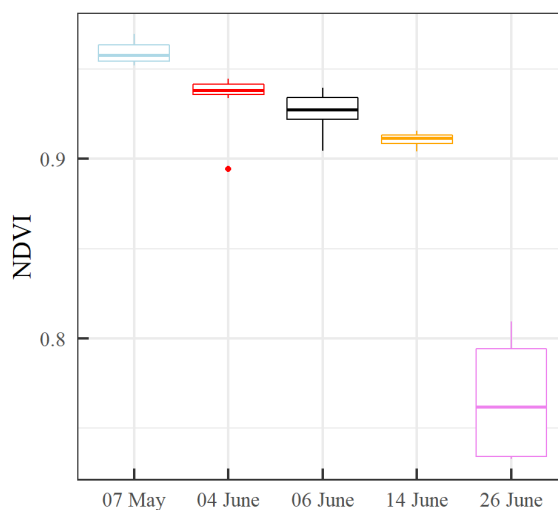


**Figure 13:** Aerial map of  $F_{760}$  (a) on 26 June 2018 with measurement locations used to combine with mobile (circles) and stationary (triangles) measurements. Diurnal changes in  $F_{760}$  on different days of the campaign (b) as 5-minute measurement averages depicted in the same colours as observation locations in a).



5

**Figure 14:** Seasonal changes of a NDVI in winter wheat field over the course of the CloudRoots campaign.

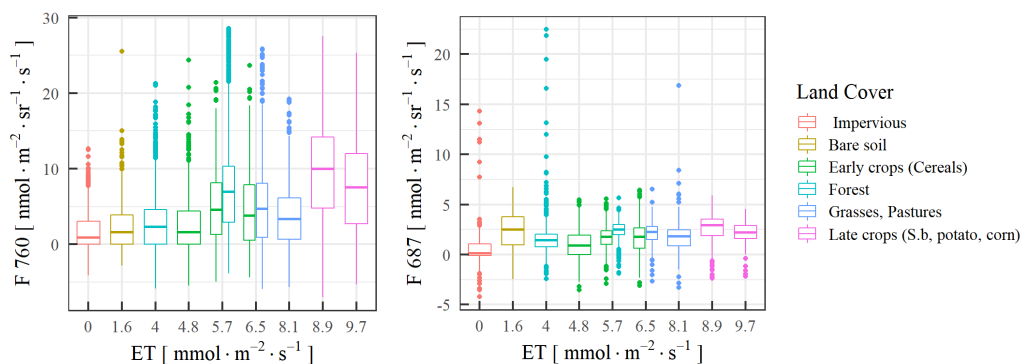


**Figure 15:** Box plot (median, min and maximum values and outliers) of the correlation between evapotranspiration and fluorescence  $F_{760}$  (left) and  $F_{687}$  (right). The data were collected on 26 June 2018. The labels of the x-axis (ET) are shown to improve the plot visualisation.

5

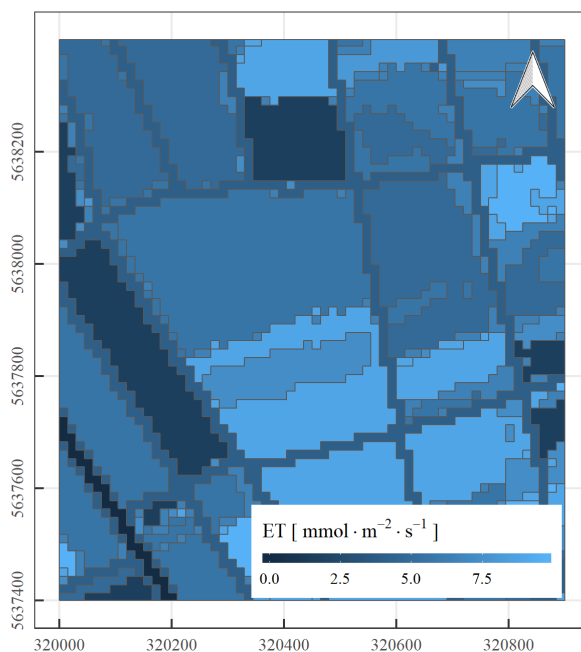


**Figure 16:** Spatial variability of evapotranspiration inferred from the fluorescence measurements combining  $K_c$  coefficients with the value of potential grass reference ET. The x- and y-axis represent the geographical coordinates of the CloudRoots site in metres (50°51'57.3"N 6°26'42.5"E).

10

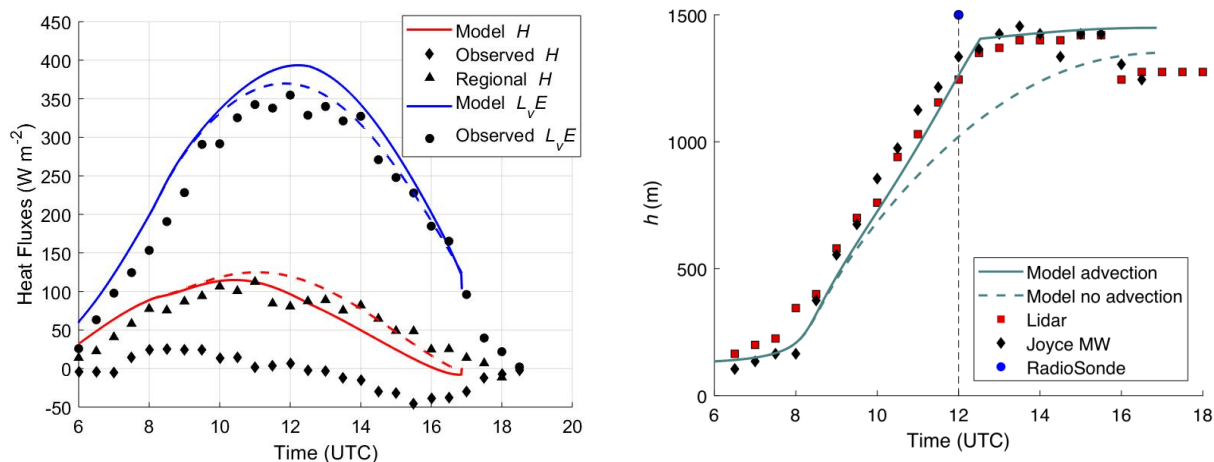


**Figure 17:** Comparison of the model and observed results of 7 May 2018: (left) surface fluxes and (right) boundary-layer depth. The regional H, an aggregate that combines the vegetated and bare soil surfaces around the CloudRoots site and shown in Fig. 1b, is also included. For the boundary-layer depth estimations, we used three different observational techniques. The LIDAR and microwave (MW) techniques were located at the JOYCE site facility. Solid and dashed lines represent the model results of surface fluxes and boundary-layer height with and without imposing the advection of heat, respectively (Table A2) for complete the information on initial and boundary conditions.

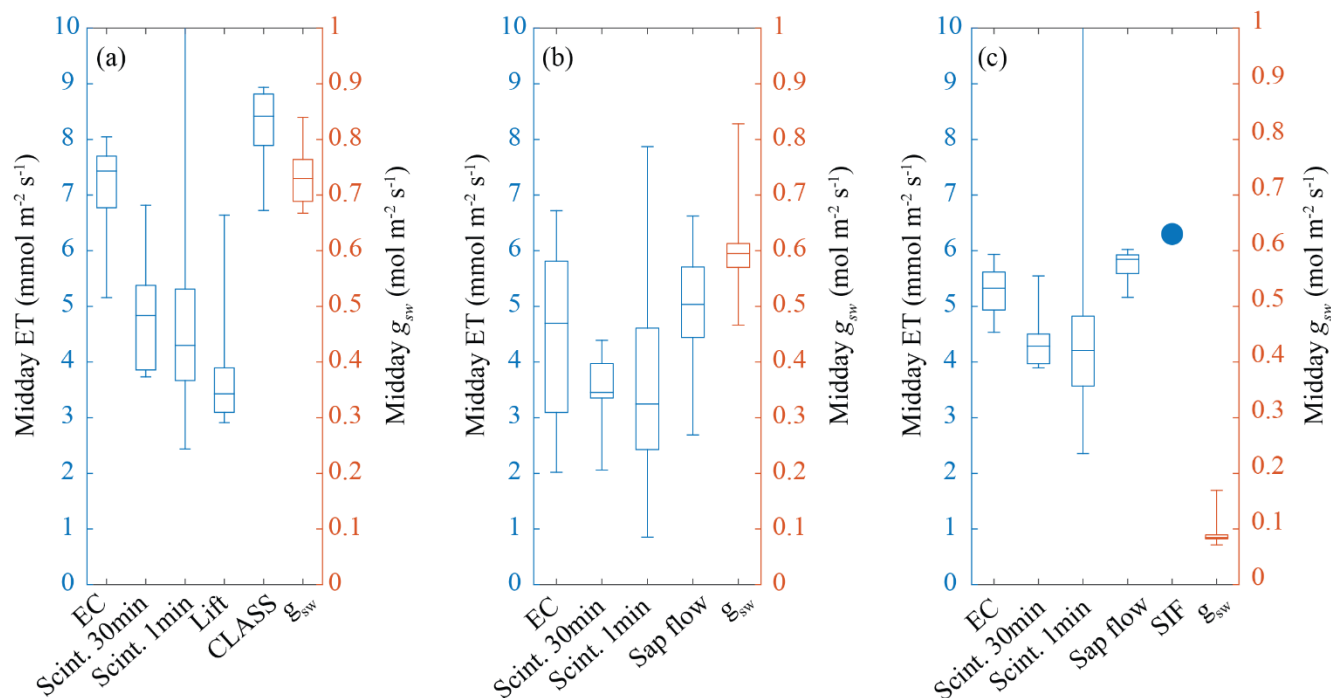


**Figure 18:** Summary of midday evapotranspiration collected using different instrumental techniques during IOP 1 (a), IOP 2 (b) and IOP 3 (c). ET fluxes (left y-axis) and  $g_{sw}$  (right y-axis) reflect the period from 09 to 14 UTC. Box plots denote the variability in 30-minute measurement intervals, except for the 1-minute scintillometer measurements. Central mark of each box indicates the median, and the bottom and top edges of the box indicate the 25th and 75th percentiles, respectively. The acronyms are eddy-covariance (EC), scintillometer (Scint) with 30-minutes (30min) and 1-minute averages, ET inferred from the lift profiles (Lift), sap flow, ET calculated with the CLASS model and ET inferred from the sun-induced fluorescence (SIF).



**Table 1:** Meteorological and biometric conditions during the intensive operation periods on 7 May (IOP 1), 15 June (IOP 2) and 28 June 2018 (IOP 3). Global radiation, vapour-pressure deficit (VPD), photosynthetically active radiation (PAR) and soil water content (SWC) are daily averages.

	IOP 1	IOP 2	IOP 3
<b>Meteorological conditions</b>			
cloud amount	0-1	3-6	0-4
temperature range (°C)	7.0 - 25.4	13.2 - 23.9	10.1 – 27.6
wind range (m s <sup>-1</sup> )	0.1 – 2.1	0.06 – 1.5	0.2 – 3.3
global radiation* (W m <sup>-2</sup> )	514	311	462
<b>Biometric conditions</b>			
canopy height (m)	0.45	0.80	0.78
LAI (m <sup>2</sup> m <sup>-2</sup> )	4.5	5.5	5.5
VPD / VPD <sub>max</sub> (kPa)	11.7 / 20.9	7.6 / 14.9	16.0 / 23.6
PAR* (μmol m <sup>-2</sup> s <sup>-1</sup> )	768	475	741
SWC 5, 20, 50 cm (vol.%)	0.20 / 0.27 / 0.30	0.17 / 0.19 / 0.22	0.12 / 0.15 / 0.21

\* Daily averages calculated from sunrise to sunset

5 **Table 2:** List of symbols, description, units and the representatively scale.

Symbol	Description	Unit	Scale represented
$A$	photosynthesis rate	μmol m <sup>-2</sup> s <sup>-1</sup> , mg m <sup>2</sup> s <sup>-1</sup>	field scale
$A_{leaf}$	leaf-level photosynthesis rate	μmol m <sup>-2</sup> s <sup>-1</sup> , mg m <sup>2</sup> s <sup>-1</sup>	leaf level
$A_m$	maximum light-saturated photosynthesis	μmol m <sup>-2</sup> s <sup>-1</sup> , mg m <sup>2</sup> s <sup>-1</sup>	field scale
$A_{m, max298}$	maximum leaf-level photosynthesis rate	μmol m <sup>-2</sup> s <sup>-1</sup> , mg m <sup>2</sup> s <sup>-1</sup>	leaf level
$E$	evaporation	mm, W m <sup>-2</sup>	
$E_{lysi}$	evaporation from microlysimeters	W m <sup>-2</sup>	field scale
$E_p$	evaporation profile based	W m <sup>-2</sup>	leaf level
$E_{sap}$	sap flow	μmol tiller <sup>-2</sup> s <sup>-1</sup>	leaf level
$ET$	evapotranspiration	mm, W m <sup>-2</sup>	
$g_{sw}$	stomatal conductance of water vapour	mol m <sup>-2</sup> s <sup>-1</sup>	
$h$	height	m	
$h_c$	canopy height	m	
$L_v E$	latent heat flux	W m <sup>-2</sup>	
$LAD$	leaf area density	m <sup>2</sup> m <sup>-3</sup>	
$LAI$	leaf area index	m <sup>2</sup> m <sup>-2</sup>	
PAR	photosynthetically active radiation	μmol m <sup>-2</sup> s <sup>-1</sup> , W m <sup>-2</sup>	
$Q^*$	net radiation	W m <sup>-2</sup>	
$R_d$	CO <sub>2</sub> dark respiration	mg m <sup>2</sup> s <sup>-1</sup>	



$R_s$	soil respiration	$\mu\text{mol m}^{-2} \text{s}^{-1}$	
$S_{\downarrow}$	global radiation	$\text{W m}^{-2}$	
$SH$	sensible heat flux	$\text{W m}^{-2}$	
$T$	temperature	$^{\circ}\text{C}, \text{K}$	
$T_{air}$	air temperature	$^{\circ}\text{C}, \text{K}$	
$T_{air,p}$	air temperature from vertical profile meas.	$^{\circ}\text{C}, \text{K}$	leaf level
$T_p$	transpiration, profile-based	$\text{W m}^{-2}$	leaf level
$u$	wind speed	$\text{m s}^{-1}$	
$u_p$	wind speed from vertical profile meas.	$\text{m s}^{-1}$	leaf level
VPD	vapour-pressure deficit	kPa	
$\alpha$	light-use efficiency	$\text{mg J}^{-1}$	field scale
$\alpha_0$	initial value of light-use efficiency	$\text{mg J}^{-1}$	field scale
$\chi_{\text{CO}_2}$	mole fractions of $\text{CO}_2$ concentration	$\mu\text{mol mol}^{-1}$	leaf level
$\chi_{\text{H}_2\text{O}}$	mole fractions of $\text{H}_2\text{O}$ concentration	$\mu\text{mol mol}^{-1}$	leaf level

**Table 3:** Parameters representing the maximum leaf-level photosynthesis rate ( $A_{m,max298}$ ) in  $\mu\text{mol m}^{-2} \text{s}^{-1}$  and the initial value of light-use efficiency ( $\alpha_0$ ) under low light, as adjusted in the original A- $g_s$  model to represent plant-specific photosynthesis characteristics.

Fitted model variable	Default value (for C3 plants)	Fitted on A- PAR and A-Ci curves	IOP 1	IOP 2	IOP 3
			maximum leaf-level photosynthesis rate ( $A_{m,max298}$ )	2.2	1.926
light-use efficiency ( $\alpha_0$ )	0.017	0.0052	0.0053	0.0053	0.0053

5

**Table 4:** Used estimated  $K_c$  coefficients for different land use (LU) classification from FAO56 combined into a new LU class.

LU classification	Introduced new LU classes	Estimated $K_c$
1 asphalt/road	impervious	0
2 bare ground	bare soil	0.2
3 cereals	early crops (cereals)	0.8
4 commercial area	impervious	0
5 coniferous trees	forest	0.5
6 copse	forest	0.7
7 country road	impervious	0



8	deciduous trees	forest	0.7
9	disposal site	impervious	0
10	electrical substation	impervious	0
11	federal motorway	impervious	0
12	federal road	impervious	0
13	maize	late crops (sugar beet, potato, corn, root crops)	1.2
14	pasture	grassland	0.8
15	potato	late crops (sugar beet, potato, corn, root crops)	1.1
16	power station (lignite)	impervious	0
17	public place/impervious surface	impervious	0
18	railroad	impervious	0
19	rapeseed	bare soil	0.2
20	road	impervious	0
21	root crops	late crops (sugar beet, potato, corn, root crops)	1.1
22	sugar beet	late crops (sugar beet, potato, corn, root crops)	1.1
23	tree nursery	forest	0.7
24	urban green area	grassland	1
25	waste disposal facility	impervious	0
26	winter barley	early crops (cereals)	0.6
27	winter wheat	early crops (cereals)	0.7

## Appendix 1

### 10 Net radiation versus latent heat under clear and cloudy conditions



For the construction of the curves in Fig. 10, the data were divided into bins of  $Q^*$ . Each bin covers a range of  $100 \text{ W m}^{-2}$ , starting at  $-200$  to  $100 \text{ W m}^{-2}$  for cloudy skies and at  $0$  to  $100 \text{ W m}^{-2}$  for clear skies. For each data point the diffuse fraction of PAR is determined by combining measurements of incoming total PAR and incoming diffuse PAR. Subsequently, a data point is labelled ‘clear’ for diffuse fractions  $< 0.3$  and labelled ‘cloudy’ for diffuse fractions  $> 0.8$ . We choose these boundaries to balance a distinct difference between clear and cloudy skies with a large enough sample size for each bin. For clear skies, the first two bins are missing. This is due to the fact that under clear skies low levels of  $Q^*$  are the result of the sun being close to the horizon, and as a result solar radiation has to travel a long distance through the atmosphere before reaching the surface. In those cases, most of the solar radiation reaches the surface as diffuse radiation due to *Rayleigh* scattering and scattering by aerosols, and therefore does not meet the criteria to be labelled “clear”. For cloudy skies, bins are missing for high levels of  $Q^*$ . Clouds attenuate solar radiation through absorption and backscattering, and thereby reduce  $Q^*$  to a level lower than it would be for a clear sky.

**Table A1:** Management activities on the test site over the winter wheat cultivation cycle before, during and after the observation period of the CloudRoots campaign.

Date	Management	Product
25 Oct 2018	sowing crop seeds	winter wheat (Premio)
8 Mar 2018	fertilisation	$81.6 \text{ kg N ha}^{-1}$
9 Apr 2018	herbicide treatment	$200 \text{ g ha}^{-1}$ Broadway
9 Apr 2018	herbicide treatment	$1 \text{ l ha}^{-1}$ CCC720
22 Apr 2018	fertilisation	$39.2 \text{ kg N ha}^{-1}$
2 May 2018	fungicide treatment	$1 \text{ l ha}^{-1}$ Capalo
2 May 2018	fungicide treatment	$0.3 \text{ l ha}^{-1}$ Corbel
2 May 2018	herbicide treatment	$0.3 \text{ l ha}^{-1}$ CCC720
16 May 2018	fertilization	$50 \text{ kg N ha}^{-1}$
19 May 2018	fungicide treatment	$1.5 \text{ l ha}^{-1}$ Adexar
19 May 2018	fungicide treatment	$0.5 \text{ l ha}^{-1}$ Diamant
19 May 2018	insecticide treatment	$0.3 \text{ l ha}^{-1}$ Bulldock
16 July 2018	harvesting	winter wheat, $92 \text{ dt ha}^{-1}$
19 July 2018	Straw pressed and removed	
25 Aug 2018	ploughing	
18 Sep 2018	harrowing	

15

**Table A2:** Initial and boundary conditions prescribed in CLASS to reproduce IOP 1 (7<sup>th</sup> May 2018).



Mixed-layer model parameters		
Parameter (units)	Value	Source
time steps (s)	60	-
runtime (s)	50400	-
residual-layer starting height (m)	135	Joyce microwave
surface layer top height (m)	1400	radiosonde
surface pressure (Pa)	100600	EC pressure gauge
large-scale wind divergence ( $s^{-1}$ )	0	default
$f_c$ ( $m s^{-1}$ )	$1.10^{-4}$	latitude
Coriolis parameter (-)	0.2	default
<i>Potential temperature</i>		
initial mixed-layer temperature (K)	286.2	profile data and radiosonde
jump in potential temperature from boundary layer to free troposphere (K)	4	radiosonde
jump in potential temperature from boundary layer to residual layer (K)	4.4	radiosonde
free troposphere lapse-rate for potential temperature ( $h < 1400$ m) (K)	$4.9 \cdot 10^{-3}$	radiosonde
free troposphere lapse-rate for potential temperature ( $h < 1400$ m) (K)	$6.2 \cdot 10^{-3}$	radiosonde
advection of heat into the mixed-layer ( $K s^{-1}$ )		$2.5 \cdot 10^{-4} e^{-\frac{(t[UTC]-12)^2}{5}}$
<i>Specific humidity</i>		
initial function mixed-layer specific humidity ( $kg kg^{-1}$ )		$0.0067 - 0.0004(t[UTC] - 6.5)$
Residual-layer lapse rate for specific humidity ( $kg kg^{-1} m^{-1}$ )	$-1.4 \cdot 10^{-3}$	radiosonde
free troposphere lapse-rate specific humidity ( $h < 1400$ m) ( $kg kg^{-1} m^{-1}$ )	$-2.7 \cdot 10^{-6}$	radiosonde
free troposphere lapse-rate specific humidity ( $h < 1400$ m) ( $kg kg^{-1} m^{-1}$ )	$-9.0 \cdot 10^{-6}$	radiosonde
advection of specific humidity into the mixed-layer ( $kg kg^{-1} m^{-1}$ )	0	default
<i>Carbon dioxide</i>		
initial mixed-layer $CO_2$ (ppm)	400	profile measurements
jump in $CO_2$ at the inversion layer (ppm)	-44	profile measurements
free troposphere lapse-rate for $CO_2$ ( $ppm m^{-1}$ )	0	default
advection of $CO_2$ into the mixed-layer ( $ppm s^{-1}$ )	0	default
<i>Wind</i>		
initial wind speed in the longitudinal direction ( $m s^{-1}$ )	1.75	profile measurements
jump in longitudinal wind velocity at the inversion layer ( $m s^{-1}$ )	3	profile measurements
free troposphere lapse-rate for longitudinal wind velocity ( $m s^{-1} m^{-1}$ )	$-1.8 \cdot 10^{-3}$	profile measurements
advection of longitudinal wind into the mixed-layer ( $m s^{-1} s^{-1}$ )	0	default
wind speed in the latitudinal direction ( $m s^{-1}$ )	0	default
jump in latitudinal wind velocity at the inversion layer ( $m s^{-1}$ )	0	default
free troposphere lapse rate for latitudinal wind velocity ( $m s^{-1} m^{-1}$ )	0	default
advection of latitudinal wind into the mixed-layer ( $m s^{-1} s^{-1}$ )	0	default



roughness length for momentum (m)	0.02	canopy height
roughness length for scalars (m)	0.002	canopy height
<i>Geographical coordinates and radiation</i>		
latitude (deg)	50.9	geographical location
longitude (deg)	6.4	geographical location
Julian day-of-year (days) (7 <sup>th</sup> May 2018)	127	data selected case
start time (hrs UTC)	6.0	-
cloud cover fraction (-)	0	camera
cloud-top radiative divergence (W m <sup>-2</sup> )	0	camera
<i>Soil</i>		
soil moisture top soil layer (m <sup>3</sup> m <sup>-3</sup> )	0.177	soil measurements
soil moisture deep soil layer (m <sup>3</sup> m <sup>-3</sup> )	0.286	soil measurements
Vegetation cover fraction (-)	0.98	visual inspection, camera
T top soil layer (K)	285.5	soil measurements
T deep soil layer (K)	284	soil measurements
Clapp & Hornberger parametre a (-)	0.219	soil composition
Clapp & Hornberger parametre b (-)	5.3	soil composition
Clapp & Hornberger parametre p (-)	4	soil composition
saturated soil conductivity for heat (-)	3.56·10 <sup>-6</sup>	soil composition
saturated volumetric water content (-)	0.472	soil composition
field capacity volumetric water content (-)	0.3	soil composition
wilting point volumetric water content (-)	0.154	soil composition
parameter to calculate top layer soil moisture tendency (-)	disabled	soil composition
parameter to calculate top layer soil moisture tendency (-)	disabled	soil composition
LAI (-)	4.5	on-site determination
correction factor transpiration for VPD for high vegetation (-)	0	vegetation height
minimum soil resistance [s m <sup>-1</sup> ]	50	default
albedo (-)	0.2	radiation measurements
surface temperature (K)	286.3	profile measurements
thickness of water layer on wet vegetation (m)	0.0002	default
equivalent water-layer depth for wet vegetation (m)	0.0001	on-site observations
thermal conductivity skin layer	5.9	default
<b>A-g, model parameters</b>		
CO <sub>2</sub> compensation concentration (mg m <sup>-3</sup> )	68.5	C3 reference value
function parameter to calculate CO <sub>2</sub> compensation (-)	1.5	C3 reference value
mesophyll conductance (m s <sup>-1</sup> )	10.0	leaf gas exchange
maximum assimilation rate for CO <sub>2</sub> at 298 K (mg m <sup>-2</sup> s <sup>-1</sup> )	1.926	leaf gas exchange
reference temperature to calculate mesophyll conductance (K)	278	C3 reference value
reference temperature to calculate mesophyll conductance (K)	301	C3 reference value
function parameter to calculate maximal primary productivity (-)	2.0	C3 reference value
reference temperature to calculate maximal primary productivity (K)	281	C3 reference value
reference temperature to calculate maximal primary productivity (K)	311	C3 reference value



maximum value of the ratio between the leaf and external (-)	0.89	C3 reference value
regression coefficient to calculate the ratio between the leaf and external CO <sub>2</sub> concentration (-)	0.07	C3 reference value
initial low-light-conditions use efficiency for CO <sub>2</sub> (mg J <sup>-1</sup> )	0.0053	leaf gas exchange
extinction coefficient PAR (m m <sup>-1</sup> )	0.7	C3 reference value
minimum cuticular conductance (mm s <sup>-1</sup> )	2.5·10 <sup>-4</sup>	C3 reference value

---